

Comparing 1-year GUMICS–4 simulations of the Terrestrial Magnetosphere with Cluster Measurements

G. Facskó^{1,2,3}, D. G. Sibeck², I. Honkonen⁴, J. Bór⁵, G. Farinas Perez^{2,3*},
A. Timár¹, Y. Y. Shprits^{6,7}, L. Degener^{4†}, P. Peitso^{8‡}, E. I. Tanskanen⁸,
C. R. Anekallu⁹, J. Kalmár⁵, S. Szalai^{5,10}, Á. Kis⁵, V. Wesztergom⁵,
N. A. Aseev^{6,7}, Á. Madár^{1,11}

¹Wigner Research Centre for Physics, Budapest, Hungary

²NASA Goddard Space Flight Center, Greenbelt, Maryland, USA

³the Catholic University of America, Washington DC, USA

⁴Finnish Meteorological Institute, Helsinki, Finland

⁵Institute of Earth Physics and Space Science, Sopron, Hungary

⁶Helmholtz Centre Potsdam, GFZ German Research Centre for Geosciences, Potsdam, Germany

⁷Institute for Physics and Astronomy, University of Potsdam, Potsdam, Germany

⁸Aalto University, School of Electrical Engineering, Espoo, Finland

⁹UCL Department of Space & Climate Physics, Mullard Space Science Laboratory, Dorking, UK

¹⁰University of Miskolc, Department of Geophysics, Miskolc, Hungary

¹¹Eötvös Loránd University, Doctoral School of Physics, Budapest, Hungary

Key Points:

- The GUMICS–4 code provides realistic ion plasma moments and magnetic field in the solar wind and the outer magnetosheath.
- The code predicts realistic bow shock locations.
- An inner magnetosphere model should be added to the code to increase the accuracy of the simulation in inner magnetosphere.

*Now at University of Miami, Electrical and Computer Engineering Department, Miami, Florida, USA

†Now private individual, Hannover, Germany

‡Now at Aurora Propulsion Technologies, Espoo, Finland

Corresponding author: Gábor Facskó, facsko.gabor@wigner.hu

24 **Abstract**

25 We compare the predictions of the GUMICS–4 global magnetohydrodynamic model for
 26 the interaction of the solar wind with the Earth’s magnetosphere **with** Cluster SC3 mea-
 27 surements over for one year, from January 29, 2002 to February 2, 2003. In particular,
 28 we compare **model predictions with** the north/south component of the magnetic field
 29 (B_z) **seen by the magnetometer**, the component of the velocity along the Sun-Earth
 30 line (V_x), and the plasma density as determined from a top hat plasma spectrometer and
 31 the spacecraft’s potential **from the electric field instrument**. We select intervals in
 32 the solar wind, the magnetosheath and the magnetosphere where these instruments pro-
 33 vided good quality data and the model correctly predicted the region in which the space-
 34 craft is located. We determine the location of the bow shock, the magnetopause and, the
 35 neutral sheet from the spacecraft measurements and compare **these** locations to those
 36 predicted by the simulation.

37 The GUMICS–4 model **agrees well with the measurements** in the solar wind
 38 however its accuracy is worse in the magnetosheath. The simulation results are not re-
 39 alistic in the magnetosphere. The bow shock location is predicted well, however, the mag-
 40 netopause location is less accurate. The neutral sheet positions are located quite **accu-**
 41 **rate** thanks to the special solar wind conditions **when the B_y component of the in-**
 42 **terplanetary magnetic field is small.**

43 **1 Introduction**

44 One of the most cost-effective ways to study the interaction of the solar wind with
 45 planetary magnetospheres (or predict [...] conditions in near-Earth space) is modeling
 46 this complex system using a magnetohydrodynamic (MHD) code. In the past, several
 47 parallelized codes were developed, which are **used for forecasting the near-Earth**
 48 **space environment**. Such as the Lyon-Fedder-Mobarry [LFM; *Lyon et al.*, 2004] code,
 49 the Grid Agnostic MHD for Extended Research Applications [GAMERA; *Zhang et al.*,
 50 2019], the Open Geospace General Circulation Model [OpenGGCM; *Raeder et al.*, 2008],
 51 **or** the Block-Adaptive-Tree-Solarwind-Roe-Upwind-Scheme [BATS-R-US; *Powell et al.*,
 52 1999; *Tóth et al.*, 2012]. In Europe [...] three global MHD codes **have been** developed:
 53 the Grand Unified Magnetosphere–Ionosphere Coupling Simulation [GUMICS–4; *Jan-*
 54 *hunen et al.*, 2012], the Computational Object Oriented Libraries for Fluid Dynamics
 55 [COOLFluiD; *Lani et al.*, 2012] and the 3D resistive magnetohydrodynamic code Gor-

gon [Chittenden *et al.*, 2004; Ciardi *et al.*, 2007]. The COOLFluiD is a general-purpose plasma simulation tool. The Gorgon code was developed to study high energy, collisional plasma interactions and has been adapted to simulate planetary magnetospheres and their interaction with the solar wind [Mejnertsen *et al.*, 2016, 2018]. Neither Gorgon nor COOLfluid have an ionospheric solver. Almost all of these codes are available at the Community Coordinated Modelling Center (CCMC; <http://ccmc.gsfc.nasa.gov/>) hosted by the NASA Goddard Space Flight Center (GSFC) or the Virtual Space Weather Modelling Centre (VSWMC; <http://swe.ssa.esa.int/web/guest/kul-cmpa-federated>; requires registration for the European Space Agency (ESA) Space Situational Awareness (SSA) Space Weather (SWE) portal) hosted by the KU Leuven [Poedts *et al.*, 2020]. A comparison of the simulation results with spacecraft and ground-based measurements is necessary to understand the abilities and features of the developed tools. A statistical study using long term global MHD runs for validation of the codes seems **necessary**. Because providing long simulations **is** costly and time consuming, only a few studies have been done, almost all for periods much less than a year except Liemohn *et al.* [2018].

Guild *et al.* [2008a,b] launched two months of LFM runs and compared the plasma sheet properties in the simulated tail with the statistical properties of six years **of** Geotail magnetic field and plasma observations [Kokubun *et al.*, 1994; Mukai *et al.*, 1994]. The LFM successfully reproduced the global features of the global plasma sheet in a statistical sense. However, there were some differences. The **predicted plasma** sheet was too cold, too dense and the bulk flow was faster than the observed plasma sheet [Kokubun *et al.*, 1994; Mukai *et al.*, 1994]. The LFM overestimated the ionospheric transpolar potential. The transpolar potential correlated with the speed of the plasma sheet flows. Equatorial maps of density, thermal pressure, thermal energy and, velocity were compared. The LFM overestimated the plasma sheet density close to the Earth, the temperature by a factor of ~ 3 and the global average flow speed by a factor of ~ 2 . The LFM reproduced many of the climatological features of the Geotail data set. The low-resolution model underestimated the occurrence of the fast earthward and tailward flows. Increasing the simulation resolution resulted in the development of fast, busty flows. These flows influenced the statistics and contributed to a better agreement between simulations and observations.

Zhang *et al.* [2011] studied the statistics of magnetosphere-ionosphere (MI) coupling using **the LFM simulation of** Guild *et al.* [2008a] above. The polar cap poten-

89 tial and the field aligned currents (FAC), the downward Poynting flux and, the vorticity
 90 of the ionospheric convection were compared with observed statistical averages and
 91 the Weimer05 empirical model [Weimer, 2005]. The comparisons showed that the LFM
 92 model produced quite accurate average distributions of the Region 1 (R1) and Region
 93 2 (R2) currents. The ionospheric R2 currents in the MHD simulation seemed to orig-
 94 inate from the diamagnetic ring current. The average LFM R1 and R2 currents were small
 95 compared with the values from the Weimer05 model. The average Cross Polar Cap Po-
 96 tential (CPCP) was higher in the LFM simulation than the measurements of the Super-
 97 DARN and the Weimer05 model. The average convention pattern was quite symmet-
 98 ric in the LFM simulation **as compared to** the SuperDARN measurements and the Weimer05
 99 model. The SuperDARN measurements and the Weimer05 model had a dawn-dusk asym-
 100 metry. In the LFM model, more Poynting flux flowed into the polar region ionosphere
 101 than in the Weimer05 model **as a** [...] consequence of the larger CPCP in the LFM sim-
 102 ulation. The larger CPCP allowed a higher electric field in the polar region. The sta-
 103 tistical dependence of the high-latitude convection patterns on Interplanetary Magnetic
 104 Field (IMF) clock angle was similar to the SuperDARN measurements [Sofko *et al.*, 1995]
 105 and the Weimer05 model. The average ionospheric field-aligned vorticity showed good
 106 agreement on the dayside. However, the LFM model gave a larger nightside vorticity than
 107 SuperDARN measurements because the Pedersen conductance on the night side iono-
 108 sphere was too low.

109 Wiltberger *et al.* [2017] studied the structure of high latitude field-aligned current
 110 patterns using three resolutions of the LFM global MHD code and the Weimer05 em-
 111 pirical model [Weimer, 2005]. The studied period was a month-long and contained two
 112 high-speed streams. Generally, the patterns agreed well with results obtained from the
 113 Weiner05 computing. As the resolution of the simulations increased, the currents became
 114 more intense and narrow. The ratio of the Region 1 (R1), the Region 2 (R2) currents
 115 and, the R1/R2 ratio increased when the simulation resolution increases. However, both
 116 the R1 and R2 currents were smaller than the predictions of the Weimer05 model. This
 117 effect led to a better agreement of the LFM simulation results with the Weimer 2005 model
 118 results. The CPCP pattern became concentrated in higher latitudes because of the stronger
 119 R2 currents. The relationship of the CPCP and the R1 looked evident at a higher res-
 120 olution of the simulation. The LFM simulation could have reproduced the statistical fea-
 121 tures of the field-aligned current (FAC) patterns.

122 *Hajducek et al.* [2017] simulated the month **of** [...] January 2005 [...] using the
123 Space Weather Modelling Framework [SWMF; *Tóth et al.*, 2005] and the OMNI solar
124 wind data (<https://omniweb.gsfc.nasa.gov/>) as input. The simulations were **executed**
125 with and without an inner magnetosphere model and using two different grid resolutions
126 **in magnetosphere**. The model was very good in predicting the ring currents [SYM-
127 H; <http://wdc.kugi.kyoto-u.ac.jp/aeasy/asy.pdf>; *Iyemori*, 1990]. The K_p index (**a** mea-
128 sure **of** the general magnetospheric convention and the auroral currents [*Bartels et al.*,
129 1939; *Rostoker*, 1972; *Thomsen*, 2004]) was predicted well during storms however the
130 index was overestimated during quiet periods. The AL index (that describes the west-
131 ward electrojet of the surface magnetic field introduced by *Davis and Sugiura* [1966]) was
132 predicted reasonably well on average. However the model reached the highest negative
133 AL value less often **than** it was reached in [...] observations because the model cap-
134 tured the structure of the auroral zone currents poorly. The overpredicting of K_p index
135 during quiet times might have had the same reason because **it is** also sensitive to au-
136 roral zone dynamics. The SWMF usually over-predicted the CPCP. These results were
137 not sensitive to grid resolutions, with the exception of the AL index, which reached the
138 highest negative value more often when the grid resolution was higher. Switching off of
139 the inner magnetosphere model had a negative effect on the accuracy of all quantities
140 mentioned above, except the CPCP.

141 This paper **compares** the Cluster SC3 measurements [...] directly to a previously
142 made 1-year long GUMICS-4 simulation **at locations** in the solar wind, magnetosheath
143 and the magnetosphere along the Cluster SC3 orbit [...] [*Facskó et al.*, 2016]. **The** pa-
144 **rameters are** [...] B_z , the north/south component of the magnetic field in GSE coor-
145 dinates, the solar wind velocity GSE X component (V_x) and the solar wind density n .
146 **We also compare the predicted and observed** locations of the bow shock, magne-
147 topause and the neutral sheet. These parameters are selected because B_z controls the
148 **solar wind-magnetosphere interaction**, V_x is the main component of the solar wind
149 velocity and n is the ion plasma **moment** that is the easiest to calculate; furthermore
150 **several** instruments could determine it (see Section 2.2). The structure of this paper
151 is as follows. Section 2 describes the GUMICS-4 code, the 1-year simulation and the
152 [...] **Cluster spacecraft measurements**. Section 3 gives comparisons between the sim-
153 **ulations** and observations. Results of the comparison are discussed in Section 4. Finally,
154 Section 5 contains the conclusions.

155 **2 The GUMICS–4 products and Cluster measurements**

156 Here we use two very different time series. The first type is derived from a **pre-**
 157 **vious** 1-year run of the GUMICS–4 simulation [Fazskó *et al.*, 2016]. The second time
 158 **series was** measured by the magnetometer, ion plasma and electric field instruments of
 159 the Cluster reference spacecraft.

160 **2.1 The GUMICS–4 code**

161 The GUMICS–4 **model** has two coupled simulation domains, the magnetospheric
 162 domain outside of **a** $3.7 R_E$ radius sphere around the Earth and a coupled ionosphere
 163 module containing **a** 2D height-integrated model of ionosphere. [...] GUMICS–4 is not
 164 a parallel code **model** however it has been extensively used **to** study [...] energy prop-
 165 agation [...] from the solar wind **into** the magnetosphere through the magnetopause
 166 and other features [Janhunen *et al.*, 2012, see the references therein]. The code has also
 167 been applied to study forced reconnection in the tail [Vörös *et al.*, 2014]. Recently, sev-
 168 eral hundred synthetic two hours duration GUMICS–4 simulation runs were made to
 169 compare the simulation results to empirical formulas [Gordeev *et al.*, 2013]. The agree-
 170 ment was quite good in general, but the diameter of the magnetopause in the simula-
 171 tions deviated **slightly (10 %)** from **corresponding** observations in the tail. The GUMICS–4
 172 simulation magnetotail was smaller than **that which** the spacecraft observed [...]. **How-**
 173 **ever, the modelled magnetopause showed good agreement with the empir-**
 174 **ical model in the midtail at northward IMF conditions.** A 1-year long simula-
 175 tion was made using the GUMICS–4 code [Fazskó *et al.*, 2016]. Juusola *et al.* [2014] com-
 176 pared the ionospheric currents, fields and the **Cross Polar Cap Potential Drop (CPCP)**
 177 in the simulation to observations from the Super Dual Auroral Radar Network (Super-
 178 DARN) radars [Greenwald *et al.*, 1995] and CHAMP spacecraft [Reigber *et al.*, 2002] **ob-**
 179 **servations of** field aligned currents (FAC) [...] [Juusola *et al.*, 2007; Ritter *et al.*, 2004].
 180 The CPCP, the FAC and other currents could not be reproduced properly. **A** possible
 181 cause **for** this poor agreement could be **the model's** low resolution in inner magneto-
 182 sphere and/or the lack of an inner magnetosphere model **accurately** incorporating the
 183 physics **of** this region. This hypothesis is supported by the result of Haiducek *et al.* [2017].
 184 Haiducek *et al.* [2017] simulated only a month-long period using a different spatial res-
 185 olution and tested the code with the inner magnetosphere model of the SWMF switched
 186 off for a special run. This run without an inner magnetosphere model made it clear that

only the CPCP parameter of the simulation agreed quite well with the measurements. This fact explained why the agreement between the Cluster SC3 and the GUMICS-4 simulations was so good as described by *Lakka et al.* [2018a,b] based on the CPCP in GUMICS-4 simulations. *Kallio and Facskó* [2015] determined plasma and magnetic field parameters along the lunar orbit from [...] *Facskó et al.* [2016]'s global MHD simulations. The parameters differed significantly **from observations** in the **magnetotail** indicating **the** need for future studies. *Facskó et al.* [2016] determined the footprint of Cluster SC3 using the 1-year simulation and the Tsyganenko T96 empirical model [*Tsyganenko*, 1995]. The agreement of the footprint was better in the Northern Hemisphere. The GUMICS-4 tail was shorter in the simulations than the observations.

A 1-year global MHD simulation was produced with the GUMICS-4 code using the OMNI solar wind data from January 29, 2002, to February 2, 2003, as input [*Facskó et al.*, 2016]. The creation and analysis of the simulation were based on a work package of the European Cluster Assimilation Technology (ECLAT) project (https://cordis.europa.eu/result/rcn/165813_en.html). The GUMICS-4 is a serial code [*Janhunen et al.*, 2012] hence the 1-year simulation was made in 1860 independent runs. This interval covered 155 Cluster SC3 orbits and each orbit lasted 57 hours. The FMI supercomputer at the time had 12 cores on each node hence the 57 hours were divided into 4.7 hours simulation time with one hour initialisation period. Each sub-interval used its own individual average Geocentric Solar Ecliptic (GSE) IMF magnetic field X component B_x component and dipole tilt angle. All data gaps in the solar wind were interpolated linearly. If the data gap of the input file was at the beginning (or the end) of the interval then the first (or last) good data from the input file was used to fill the gap. The initialization of each simulation run was made using constant values. These values were the first valid data of the input file repeated 60 times (60 minutes) in the input file of the sub-interval. The simulation results were saved every five minutes. Various simulation parameters, for example, the density, particle density, temperature, magnetic field, solar wind velocity (29 different quantities) were saved from the simulation results along the Cluster reference spacecraft's orbit in the GSE coordinates.

2.2 The Cluster SC3 measurements

The Cluster-II **mission** of the European Space Agency (ESA) **was** launched in 2000 **to observe** geospace [*Credland et al.*, 1997; *Escoubet et al.*, 2001]. The four spacecraft

form a tetrahedron in space however here we use only the measurements of the reference spacecraft, Cluster SC3. The spacecraft were **spin** stabilized and their **rotation** period is ~ 4 s. Hence, the intrinsic time resolution of the plasma instruments is 4 s and we use 4 s averaged magnetic field data. The highest resolution of the Cluster FluxGate Magnetometer (FGM) magnetic field instrument is 27 Hz [Balogh *et al.*, 1997, 2001]. The ion plasma data are provided by the Cluster Ion Spectrometry (CIS) Hot Ion Analyser (HIA) sub-instrument [Reme *et al.*, 1997; Rème *et al.*, 2001]. The CIS HIA instrument is calibrated using the Waves of High frequency Sounder for Probing the Electron density by Relaxation (WHISPER) wave instrument onboard Cluster [Décréau *et al.*, 2001; Trotignon *et al.*, 2010; Blagau *et al.*, 2013, 2014]. The results of these calibrations can **appear** as sudden non-physical jumps in the CIS HIA data. The CIS HIA had different modes to measure in the solar wind and the magnetosphere. When the instrument switched from one mode to another mode [...] non-physical jumps also appear in the measurements. These features impair the accuracy of data analyses.

We **remove non-physical jumps from** our results [...] using a density determination based on different principles. We use the spacecraft potential of the Electric Field and Wave Experiment [EFW ; Gustafsson *et al.*, 1997, 2001] to determine the electron density. This quantity can be calculated using the empirical density formula

$$n_{EFW} = 200(V_{sc})^{-1.85}, \quad (1)$$

where n_{EFW} is the calculated density and V_{sc} is the Cluster EFW spacecraft potential [Trotignon *et al.*, 2010, 2011]. The EFW and the WHISPER were used for the calibration of the CIS HIA and the Plasma Electron and Current Experiment [PEACE; Johnstone *et al.*, 1997; Fazakerley *et al.*, 2010a,b]. Both instruments were still working onboard all Cluster spacecraft. Their stable operation reduced the number of data gaps, and it also made the data analysis easier.

3 Comparison of measurements to simulation

The parameters saved from the GUMICS–4 simulations and the Cluster SC3 magnetic field, solar wind velocity and, density measurements are compared in different regions, namely the solar wind, magnetosheath, and magnetosphere **via** cross–correlation calculations. The temporal resolution of the simulated Cluster orbit data is mostly five minutes because the results of the simulations are saved every five minutes [Facskó *et al.*,

249 2016]. However, the time difference between points can be more than five minutes at the
 250 boundary of the subintervals, because the length of the simulation intervals is determined
 251 in minutes. To facilitate analysis of the simulation results, all simulation data were in-
 252 terpolated to a one–minute resolution. This method does not provide extra information
 253 to the cross–correlation calculation. The data gaps are eliminated using linear interpo-
 254 lation and extrapolation when the gap is at the start or the end of the selected interval.
 255 The spin resolution (4 s) of Cluster SC3 magnetic field measurements is averaged over
 256 five minutes around (± 150 s) the timestamps of the saved data. Then the averaged data
 257 were interpolated to a one–minute resolution to make [...] the correlation calculations.

258 For the correlation calculation, intervals are selected carefully in the solar wind (see
 259 Section 3.1), the magnetosheath (see Section 3.2), the dayside and the night side mag-
 260 netosphere (see Section 3.3). In these intervals, the parameters did not vary a lot and
 261 we **exclude intervals when either Cluster or the virtual probe** [...] cross any bound-
 262 aries. To compare the B_z magnetic field, V_x solar wind speed and the n_{CIS} and the n_{EFW}
 263 curves we cross correlate selected intervals. We carefully examine such cases and remove
 264 intervals which are **shorter than four hours** for the ± 60 minutes correlation calcula-
 265 tion [...] and **intervals with** large data gaps from the correlation calculation. Those
 266 intervals are also **excluded when** the plasma instrument has a calibration error or a
 267 change in its recording mode as it moves from the magnetosphere to solar wind (for ex-
 268 ample). The electron density is also calculated using Equation 1 and correlated. We want
 269 to avoid the calibration errors and sudden non-physical jumps mentioned previously. The
 270 correlation results for the density derived from the electric field potential results do not
 271 differ significantly from those for the top hat plasma instrument, however the **EFW's**
 272 **n_{EFW} experiences no** mode changes and it is applicable in the magnetosphere too (**in**
 273 **contrast to** the CIS HIA instrument).

274 3.1 Solar wind

275 We use OMNI IMF and solar wind velocity, density, and temperature data as in-
 276 put to the simulation. **Comparing parameters obtained from the simulation and**
 277 **from the measurements in the solar wind region is especially interesting be-**
 278 **cause the IMF X component cannot be given to the GUMICS–4 as input** [*Janhunen*
 279 *et al.*, 2012; *Facskó et al.*, 2016]. However, the magnetic field of the solar wind has an
 280 X component in the simulations. Additionally, [...] solar wind structures might **evolve**

from the simulation domain boundary at $+32 R_E$ to the sub-solar point of the terrestrial bow shock where all OMNI data is shifted. Almost the same solar wind time intervals are used as in Table 1 of *Facskó et al.* [2016]. **Although the Cluster instruments were calibrated in 2002, just after launch, there are not many CIS HIA moment observations in 2001 and 2002** (Table 1). Hence, we do not have a satisfactory ion plasma data coverage for this year. Additionally, to improve the accuracy of the correlation calculation (see below) we **omitted** [...] intervals [...] (shorter than five hours) **and those in which** the CIS HIA instrument changed its mode. The Cluster fleet is located in the solar wind only from December to May and only for a couple of hours during each orbit near apogee. We double-check whether [...] Cluster SC3 **remains** in the solar wind in both the simulation and reality. We also check the omnidirectional CIS HIA ion spectra on the Cluster Science Archive (CSA; <https://www.cosmos.esa.int/web/csa/csds-quicklook-plots>). The spectra must contain one narrow band in the solar wind region, **indicating an observation of the solar wind beam**. Hence, **there are only 17 solar wind intervals** [...] to study, as shown in Figure 1.

The selected intervals occur for quiet solar wind conditions (Figure 2). The GUMICS-4 simulation results have five minute **time** resolution and the Cluster SC3 measurements have one minute **time** resolution (Figure 3). The measurements vary significantly. In spite of the quiet conditions the **observed** solar wind density often changes and deviates from the simulation. Figure 4c shows that both densities deviate significantly. The CIS HIA density **variations are even** larger as expected given the complexity and the large number of working modes of the CIS instrument. The magnetic field and the solar wind velocity fit better. Figure 5a shows that the correlation of the magnetic fields is very good; furthermore on Figure 5c, 5e, 5g the correlation of the solar wind velocity and density is excellent (Table 1). The time shift in Figure 5b, Figure 5d, Figure 5f is about five minutes for the magnetic field and the CIS data. On Figure 5h for the EFW data the time shift is less stable. It is not as well determined as in case of the other parameters.

309 3.2 Magnetosheath

[...] Cluster SC3 spent only a little time in the solar wind from December, 2002 to May, 2003. However, the spacecraft enters the magnetosheath each orbit (Figure 6). We **select** intervals when the value of the magnetic field is around 25 nT. The field should

be fluctuating because of the turbulent deflected flow of the shocked solar wind the temperature should be greater than that in the solar wind. The velocity should decrease to values ranging from 100-300 km/s. The density of the plasma should increase and **reach** values of 10-20 cm⁻³. The narrow band on the omnidirectional CIS HIA ion spectra from the CSA (<https://www.cosmos.esa.int/web/csa/csds-quicklook-plots>) widens from the solar wind to the magnetosheath. 15–30 minutes from each bow shock crossing we considered the Cluster SC3 to have entered into the magnetosheath. At the inner magnetopause boundary of the magnetopause the flow speed and the density drop. The magnetic field strength increases and the magnetic field becomes less turbulent than in the magnetosheath. The wide band **in** the omnidirectional CIS HIA ion spectra disappears, **indicating the plasma has undergone heating.** 15-30 minutes before (**or after**) the appearance of these indicators of the magnetopause crossing our intervals end. All intervals contain large data gaps, non-physical jumps in instrument modes or lasting less than four hour are removed. Hence, 74 intervals considered in our final selection (Table 2).

All intervals have quiet upstream (or input) solar wind conditions (Figure 7). In spite of our selected **quiet** magnetic field and plasma parameters and the calculated empirical density indicate that they vary significantly stronger than in the solar wind intervals (Figure 8). The deviation between the simulated and the observed data is also larger in this region **than in the solar wind region.** The scatter plots of the magnetic field, plasma flow speed and the densities show that these parameters agree well, but with greater variation than the scatter plots for the **same parameters in the** solar wind (Figure 9a, 9b, 9c). The correlation of the simulated and the observed data is good for the magnetic field (Figure 10a), very good for the ion plasma moments and the calculated density (Figure 10c, 10e, 10g). The timeshift of the magnetic field is within five minutes mostly (Figure 10b) however the timeshift of the ion plasma moments is scattered (Figure 10d, 10f). The timeshift of the calculated EFW density seems to be more stable (Figure 10h). Generally, the GUMICS–4 is less accurate in the magnetosheath than in the solar wind. The modelled magnetic field is **better predicted** than the modelled plasma parameters are. The calculated empirical EFW density (n_{EFW}) fits better than the CIS HIA density (n_{CIS}).

344 **3.3 Magnetosphere**

345 **We select intervals in the magnetosphere based on CIS HIA omnidirectional**
 346 **ion flux spectrum. Magnetosphere is defined by the disappearance of hot mag-**
 347 **netosheath ion population.** The plasma density decreases toward zero, the magnetic
 348 field strength **becomes** large. We **eliminated** 15–30 min after/before the magnetopause
 349 transition to identify magnetosphere intervals. This way we found 132 intervals in the
 350 magnetosphere (Table 3) using Cluster SC3 measurements. Cluster SC3 spends consid-
 351 erable time in the magnetosphere (Figure 11).

352 Here we show neither any correlation calculation nor comparison plot. In the mag-
 353 netosphere, the GUMICS–4 does not work well. Neither the magnetic field nor the plasma
 354 moments nor the N_{EFW} fit well. The solar wind velocity does not reach zero in the sim-
 355 ulation. Instead, the solar wind enters the night side magnetosphere. The solar wind CIS
 356 HIA ion plasma density and the calculated density from spacecraft potential increase closer
 357 to the Earth (plasmasphere). The GUMICS–4 density is low there. We calculated the
 358 dipole field in GSE using Tsyganenko Geotool box [Tsyganenko, 1995] and subtracted
 359 from both the observed and the simulated magnetic field B_z data. The correlation of these
 360 corrected magnetic field measurements and simulations is very low too.

361 **3.4 Bow shock, magnetopause, neutral sheet locations**

362 **We select** 77 intervals ... when Cluster SC3 crossed the terrestrial bow shock once
 363 or multiple times (Table 4). When the spacecraft crosses the bow shock inbound the mag-
 364 nitude of the magnetic field and the solar wind density increases by a factor **to** 4–5 times
 365 (from 5 nT **to** 25 nT, respectively), the solar wind speed drops from 400–600 km/s to
 366 100–300 km/s; furthermore the narrow band **in** the omnidirectional Cluster CIS HIA ion
 367 spectra widens. Both the Cluster measurements and the GUMICS–4 simulations have
 368 5-min resolution and are interpolated to 1-min resolution. All bow shock transitions of
 369 the virtual spacecraft are slower and smoother. Additionally, **GUMICS-4 does not**
 370 **predict** multiple bow shock transitions. The code reacts slowly to such sudden changes.
 371 The magnetic signatures fit better than the calculated plasma moments. The jump of
 372 the ion plasma parameters and the derived Cluster EFW density of the simulations are
 373 shifted to the measurements. Generally, the density and the velocity of the simulations
 374 seem to be less accurate than the magnetic field **in** the simulations.

54 intervals are selected around magnetopause crossings (Table 5). When the space-craft crosses the magnetopause inbound the magnitude of the magnetic field increases, the solar wind speed drops from 100–300 km/s to zero, the plasma density becomes zero; furthermore the wide band on the omnidirectional Cluster CIS HIA ion spectra disappears. The location of the magnetopause is well determined by the Cluster SC3 measurements. However, it is very difficult to identify the magnetopause crossings in the simulation data. The magnetopause crossings **usually (92 %)** cannot be seen in the simulations. **The magnetopause crossings are not visible in V_x and n . This observation is independent to the IMF orientation.** Or when the magnetopause crossings are identified in both simulations and spacecraft measurements the events are shifted **in time and location**. The accuracy of the model is lower for the dayside magnetopause locations **than the bow shock locations**.

Nine intervals are chosen around Cluster SC3 neutral sheet crossings (Figure 12; Table 6). The neutral sheet locations are determined using the results of the Boundary Layer Identification Code (BLIC) Project [Facsikó *et al.*, in preparation]. The BLIC code determines the neutral sheet crossing Cluster FGM magnetic field measurements using Wang and Xu [1994]’s method. When the solar wind speed is **very low around the currents sheet in the simulation space**; furthermore the CIS HIA density and the EFW calculated density are **very low near to the current sheet** too; finally the GSE Z component of the magnetic field changes is a sign of the code indicated neutral sheet crossing (Figure 13; red and blue curves). The neutral sheet crossings are **clearly visible** [...] in the GUMICS simulations (Figure 13; black curves). For five events (from nine Cluster SC3 crossings) the GUMICS–4 also provides similar smoothed parameters and change of sign of the B_z component. This is **an outstanding result** because the tail in the GUMICS–4 simulations is significantly smaller than [...] observed **in reality** [Gordeev *et al.*, 2013; Facsikó *et al.*, 2016]; furthermore the solar wind enters the tail in MHD simulations generally [Kallio and Facsikó, 2015].

4 Discussion

The agreement of B_z , V_x and n_{EFW} in the solar wind with the similar GUMICS simulation predictions is very good (Figure 4a, 4b, 4c, blue). The agreement of n_{CIS} is worse (Figure 4c, red). It was expected because the n_{EFW} depends on the spacecraft potential provided by the EFW instrument. However, the CIS instrument has many modes

for measuring the plasma parameters and it needs periodic calibration too. The correlation of the solar wind V_x , n_{CIS} and n_{EFW} with the similar GUMICS simulation parameters is greater than 0.9 (Figure 5c, 5e, 5g). The correlation of the B_z is also greater than 0.8 (Figure 5a). The upstream boundary of the GUMICS–4 code lies at $32 R_E$ [Jan-hunen *et al.*, 2012], the nose of the terrestrial bow shock is at about $20 R_E$. If the solar wind speed is 400 km/s, then this spatial distance means less than a 5 minutes delay, so it should not be visible in the time delays from the cross correlations. 80% of the intervals support this theory but 20% do not. In these cases, the one-minute resolution B_z , n_{CIS} or the n_{EFW} parameters have a sudden jump or variation that the simulation cannot follow, or the resolution of the simulation output (5 minutes) is too small to see these variations. Therefore, the correlation calculation is not accurate in these cases. Previously the OMNI data was compared to the Cluster data and the Cluster measurements were compared to the GUMICS–4 [Facsikó *et al.*, 2016]. The comparison suggests that the GUMICS–4 results should be similar to the OMNI data. Furthermore, we calculate correlation functions in the solar wind, where there is no significant perturbation of the input parameters in the simulation box. Therefore, we get the expected result after comparing the two different correlation calculations.

In the magnetosheath we get worse agreement with the GUMICS simulation data (Figure 9a, 9b, 9c). While the parameters are correlated, the scatter is greater. The general reason for this larger uncertainty seems to be that the magnetosheath is turbulent. This phenomenon explains the higher variations of the B_z magnetic field on Figure 9a. The solar wind V_x , n_{CIS} and n_{EFW} agree better than the magnetic field component (Figure 9b, 9c). Here there is no deviation between the densities derived in different ways (n_{CIS} and n_{EFW}) on Figure 9c. Figure 10 seems to contradict these statements above. The larger uncertainty of the B_z is visible in Figure 10a. However, that correlation is still good in Figure 10b. The other parameters have larger (> 0.9) correlation in Figure 10c, 10e, 10g. However, the time shifts in Figure 10d, 10f, 10h seem to be worse. Here the time shifts are worse because the shape of the time series in the magnetosheath looks very smooth and similar hence there are not enough points to get a sharp and large maximum correlation as the function of timeshift. The difference between the minimum and the maximum of the correlation is small compared with the uncertainty of the calculation. The maximum, the timeshift could be anywhere and the shape of the correlation vs. timeshift function is often neither symmetric nor has only one local maximum. Hence,

440 the correlation calculation provides larger time shifts for the ion plasma parameters and
 441 the n_{EFW} .

442 In the magnetosphere the GUMICS–4 does not work well. GUMICS–4 uses a tilted
 443 dipole to describe the terrestrial magnetic field [Janhunen *et al.*, 2012]. After removing
 444 the magnetic dipole from the magnetic field measurements of the Cluster SC3 and the
 445 simulation we get very low correlations and unacceptable time shifts (not shown). The
 446 tilted dipole is an insufficient description of the inner magnetospheric magnetic field. The
 447 plasma moments and the n_{EFW} do not fit either. The single fluid, ideal MHD does not
 448 describe the inner magnetosphere well therefore V_x and n in the simulations do not agree
 449 with V_x , n_{CIS} and the n_{EFW} measured by the Cluster SC3. Within the $3.7 R_E$ domain
 450 ring current physics must be added, as it has been in other global MHD codes [for ex-
 451 ample Tóth *et al.*, 2012]. This can explain the limited accuracy of the cross polar cap
 452 potential (CPCP) and geomagnetic indices of the GUMICS simulations [Juusola *et al.*,
 453 2014]. The CPCP GUMICS agrees well with spacecraft measurements therefore this quan-
 454 tity could be used for simulation studies [Lakka *et al.*, 2018a]. Haiduček *et al.* [2017] also
 455 compared geomagnetic indices and the CPCP. The Space Weather Modelling Framework
 456 (SWMF) was tested. When the inner magnetosphere model was switched off in the sim-
 457 ulation only the comparison of the simulated and observed CPCP was good. Therefore,
 458 the reason of the discrepancy of the geomagnetic indices in the GUMICS simulations must
 459 be the missing inner magnetosphere model.

460 The reason [...] why simulation results and measurements disagree could be the
 461 code or [...] bad input parameters. During the 1-year run the distributions of the OMNI
 462 solar wind magnetic field B_x , B_y , B_z components; solar wind velocity V_x , V_y V_z com-
 463 ponents and the solar wind P dynamic pressure are calculated from January 29, 2002
 464 to February 2, 2003 in GSE reference frame. These distributions of the OMNI solar wind
 465 magnetic field B_x , B_y , B_z components were overplotted by red in Figure 14a, 14d, 14g, 14j
 466 and Figure 17a, 17d, 17g, 17j; Figure 14b, 14e, 14h, 14k and Figure 17b, 17e, 17h, 17k;
 467 furthermore Figure 14c, 14f, 14i, 14l and Figure 17c, 17f, 17i, 17l. These distributions
 468 of the OMNI solar wind velocity V_x , V_y , V_z components were overplotted by red in Fig-
 469 ure 15a, 15d, 15g, 15j and Figure 18a, 18d, 18g, 18j; Figure 15b, 15e, 15h, 15k and Fig-
 470 ure 18b, 18e, 18h, 18k; furthermore Figure 15c, 15f, 15i, 15l and Figure 18c, 18f, 18i, 18l.
 471 These distributions of the P solar wind pressure calculated from the OMNI solar wind
 472 parameters were overplotted by red in Figure 16a, 16b, 16c, 16d and Figure 19a, 19b, 19c, 19d.

The intervals when the GUMICS–4 simulations and the Cluster SC3 measurements disagreed are collected for intervals in the solar wind (Table 7) and the magnetosheath (Table 8). The definition of disagreement of the simulations and measurements is quite arbitrary. When the two curves deviate or the correlation function is not symmetric we considered the simulations and the measurements disagreeing. The correlations correlation coefficients are also high in this cases however the time shift is large (~ 60 min). The averaged shifted OMNI parameters of the poorly agreeing intervals from the Tables 7 and 8 are saved. The distributions of the OMNI parameters belonging to the bad simulation results are calculated for the solar wind region (Figure 14, 15 and 16) and in the magnetosheath (Figure 17, 18 and 19).

1. In the solar wind the distributions of the OMNI B_x , B_y and B_z can be compared in Figure 14a, 14d, 14g, 14j; Figure 14b, 14e, 14h, 14k; furthermore in Figure 14c, 14f, 14i, 14l.

(a) When the B_z disagrees in simulations and measurements in Figure 14a, 14b, 14c the black and red distributions of the OMNI B_x , B_y and B_z are not similar. The reason of these strange spikes is that there is only one poorly correlated interval for the B_z in the solar wind according to Table 7.

(b) When the V_x disagrees in simulations and measurements in Figure 14d, 14e, 14f the black and red distributions of the OMNI B_x , B_y and B_z are similar. The distributions do not agree perfectly because in Table 7 the number of the poorly correlated intervals is only six for the V_x component.

(c) When the n_{CIS} disagrees in simulations and measurements in Figure 14g, 14h, 14i the black and red distributions of the OMNI B_x , B_y and B_z are similar. The distributions do not agree perfectly because in Table 7 the number of the poorly correlated intervals is only 12 for the n_{CIS} .

(d) When the n_{EFW} disagrees in Figure 14j, 14k, 14l the black and red distributions of the OMNI B_x , B_y and B_z are similar. The distributions do not agree perfectly because in Table 7 the number of the poorly correlated intervals is only nine for n_{EFW} .

The values of the OMNI B_x , B_y , and B_z are not peculiar in the solar wind.

2. In the solar wind the distributions of the OMNI V_x , V_y and V_z can be compared in Figure 15a, 15d, 15g, 15j; Figure 15b, 15e, 15h, 15k; furthermore in Figure 15c, 15f, 15i, 15l.

- 504 (a) When the B_z disagrees in Figure 15a, 15b, 15c the black and red distributions
 505 of the OMNI V_x , V_y and V_z are not similar. The reason of these strange spikes
 506 is that there is only one poorly correlated interval for the B_z in the solar wind
 507 according to Table 7.
- 508 (b) When the V_x disagrees in simulations and measurements in Figure 15d, 15e, 15f
 509 the black and red distributions of the OMNI V_x , V_y and V_z are similar. The dis-
 510 tributions do not agree perfectly because in Table 7 the number of the poorly
 511 correlated intervals is only six for the V_x component.
- 512 (c) When the n_{CIS} disagrees in Figure 15g, 15h, 15i the black and red distributions
 513 of the OMNI V_x , V_y and V_z are similar. The distributions do not agree perfectly
 514 because in Table 7 the number of the poorly correlated intervals is only 12 for
 515 the n_{CIS} .
- 516 (d) When the n_{EFW} disagrees in simulations and measurements in Figure 15j, 15k, 15l
 517 the black and red distributions of the OMNI V_x , V_y and V_z are similar. The dis-
 518 tributions do not agree perfectly because in Table 7 the number of the poorly
 519 correlated intervals is only nine for the n_{EFW} .

520 The values of the OMNI V_x , V_y , and V_z are not peculiar in the solar wind.

521 3. In the solar wind the distributions of the solar wind P calculated from OMNI pa-
 522 rameters can be compared in Figure 16a, 16b, 16c, 16d.

- 523 (a) When the B_z disagrees in Figure 16a the black and red distributions of the OMNI
 524 P are not similar. The reason of these strange spike is that there is only one
 525 poorly correlated interval for the B_z in the solar wind according to Table 7.
- 526 (b) When the V_x disagrees in simulations and measurements in Figure 16b the black
 527 and red distributions of the OMNI P are similar. The distributions do not agree
 528 perfectly because in Table 7 the number of the poorly correlated intervals is only
 529 six V_x component.
- 530 (c) When the n_{CIS} disagrees in simulations and measurements in Figure 16c the
 531 black and red distributions of the OMNI P are similar. The distributions do
 532 not agree perfectly because in Table 7 the number of the poorly correlated in-
 533 tervals is only 12 for the n_{CIS} .
- 534 (d) When the n_{EFW} disagrees in simulations and measurements in Figure 16d the
 535 black and red distributions of the OMNI P are similar. The distributions do

536 not agree perfectly because in Table 7 the number of the poorly correlated in-
 537 tervals is only nine for the n_{EFW} .

538 The values of the OMNI P are not peculiar in the solar wind.

539 4. In the magnetosheath the distributions of the OMNI B_x , B_y and B_z can be com-
 540 pared in Figure 17a, 17d, 17g, 17j; Figure 17b, 17e, 17h, 17k; furthermore in Fig-
 541 ure 17c, 17f, 17i, 17l.

542 (a) When the B_z disagrees in simulations and measurements in Figure 17a, 17b, 17c
 543 the black and red distributions of the OMNI B_x , B_y and B_z are similar.

544 (b) When the V_x disagrees in simulations and measurements in Figure 17d, 17e, 17f
 545 the black and red distributions of the OMNI B_x , B_y and B_z are similar.

546 (c) When the n_{CIS} disagrees in simulations and measurements in Figure 17g, 17h, 17i
 547 the black and red distributions of the OMNI B_x , B_y and B_z are similar.

548 (d) When the n_{EFW} disagrees in Figure 17j, 17k, 17l the black and red distribu-
 549 tions of the OMNI B_x , B_y and B_z are similar.

550 The distributions agree quite well because in Table 8 the number of the poorly
 551 correlated intervals 18, 50, 33 and 30 for the B_z , the V_x , the n_{CIS} and n_{CIS} com-
 552 ponents, respectively. The number of cases is higher and the values of the OMNI
 553 B_x , B_y and B_z are not peculiar in the magnetosheath.

554 5. In the magnetosheath the distributions of the OMNI V_x , V_y and V_z can be com-
 555 pared in Figure 18a, 18d, 18g, 18j; Figure 18b, 18e, 18h, 18k; furthermore in Fig-
 556 ure 18c, 18f, 18i, 18l.

557 (a) When the B_z disagrees in Figure 18a, 18b, 18c the black and red distributions
 558 of the OMNI V_x , V_y and V_z are similar.

559 (b) When the V_x disagrees in simulations and measurements in Figure 18d, 18e, 18f
 560 the black and red distributions of the OMNI V_x , V_y and V_z are similar.

561 (c) When the n_{CIS} disagrees in Figure 18g, 18h, 18i the black and red distributions
 562 of the OMNI V_x , V_y and V_z are similar.

563 (d) When the n_{EFW} disagrees in simulations and measurements in Figure 18j, 18k, 18l
 564 the black and red distributions of the OMNI V_x , V_y and V_z are similar.

565 The distributions agree quite well because in Table 8 the number of the poorly
 566 correlated intervals 18, 50, 33 and 30 for the B_z , the V_x , the n_{CIS} and n_{CIS} com-

567 ponents, respectively. The number of cases is higher and the values of the OMNI
 568 V_x , V_y and V_z are not peculiar in the magnetosheath.

569 6. In the magnetosheath the distributions of the solar wind P calculated from OMNI
 570 parameters can be compared in Figure 19a, 19b, 19c, 19d.

571 (a) When the B_z disagrees in Figure 19a the black and red distributions of the OMNI
 572 P are similar.

573 (b) When the V_x disagrees in simulations and measurements in Figure 19b the black
 574 and red distributions of the OMNI P are similar.

575 (c) When the n_{CIS} disagrees in simulations and measurements in Figure 19c the
 576 black and red distributions of the OMNI P are similar.

577 (d) When the n_{EFW} disagrees in simulations and measurements in Figure 19d the
 578 black and red distributions of the OMNI P are similar.

579 The distributions agree quite well because in Table 8 the number of the poorly
 580 correlated intervals 18, 50, 33 and 30 for the B_z , the V_x , the n_{CIS} and n_{CIS} com-
 581 ponents, respectively. The number of cases is higher and the values of the OMNI
 582 P are not peculiar in the magnetosheath.

583 The inaccuracy of the GUMICS-4 simulations does not depend on the OMNI parame-
 584 ters in the solar wind and magnetosheath regions. The same study does not need to be
 585 done for the magnetosphere because the deviation of the measurements and the simu-
 586 lations are so large that it cannot be caused by [...] wrong OMNI solar wind param-
 587 eters.

588 The bow shock positions agree in the GUMICS simulations and the Cluster SC3
 589 measurements. However, the magnetopause locations do not **match as** well as the bow
 590 shock in simulations and observations. In simulations the location of the magnetopause
 591 is determined from peaks in currents density, particle density gradient, or changes in flow
 592 velocity [Siscoe *et al.*, 2001; García and Hughes, 2007; Gordeev *et al.*, 2013, see references
 593 therein]. **Here** the previously saved simulation parameters along the virtual Cluster SC3
 594 orbit are analysed. The J_y current density component cannot **readily be determined**
 595 **from measurements by a single spacecraft**. Therefore, the above mentioned meth-
 596 ods cannot be applied. This discrepancy of the magnetopause location agrees with the
 597 results of Gordeev *et al.* [2013] and Facskó *et al.* [2016]. Gordeev *et al.* [2013] compared
 598 synthetic GUMICS runs with an empirical formula for the magnetopause locations. Facskó

599 *et al.* [2016] used OMNI solar wind data as input and got the same result as *Gordeev et al.*
 600 [2013] and this paper. The neutral sheets are visible in both simulations and observa-
 601 tions (Figure 13, Table 6). This experience is exceptional because the night side mag-
 602 netosphere of the GUMICS–4 simulations is small and twisted [*Gordeev et al.*, 2013; *Facskó*
 603 *et al.*, 2016]. However, in these cases the IMF has no large B_y component. From *Facskó*
 604 *et al.* [2016] we know that the GUMICS has normal long tail (or night side magnetosphere)
 605 if the B_y is small. **The code can identify the bow shock transitions clearly. For**
 606 **the magnetopause and the neutral sheet the results are more complex.**

607 5 Summary and conclusions

608 Based on the previously created 1-year long GUMICS–4 run global MHD simu-
 609 lation results are compared with Cluster SC3 magnetic field, solar wind velocity and den-
 610 sity measurements along the spacecraft orbit. Intervals are selected when the Cluster SC3
 611 and the virtual space probe are situated in the solar wind, magnetosheath and the mag-
 612 netosphere and their correlation are calculated. Bow shock, magnetopause and neutral
 613 sheet crossings are selected and their visibility and relative position are compared. We
 614 achieved the following results:

- 615 1. In the solar wind the correlation coefficient of the B_z , the V_x , the n_{EFW} and the
 616 n_{CIS} are larger than 0.8, 0.9, 0.9 and 0.9, respectively. The agreement of the B_z ,
 617 the V_x and the n_{EFW} is very good, furthermore the agreement of the n_{CIS} is also
 618 good.
- 619 2. In the magnetosheath the correlation coefficient of the B_z , the V_x , the n_{EFW} and
 620 the n_{CIS} are larger than 0.6, 0.9, 0.9 and 0.9, respectively. The agreement of the
 621 magnetic field component, the ion plasma moments and the calculated empirical
 622 density is a bit **weaker** than in the solar wind. The V_x , the n_{EFW} and the n_{CIS}
 623 fits better than the B_z component in the magnetosheath. Their agreement is still
 624 good. The reason of the deviation is the turbulent behavior of the slowed down
 625 and thermalised turbulent solar wind.
- 626 3. In neither the dayside nor the nightside magnetosphere can the GUMICS–4 pro-
 627 vide realistic results. The simulation outputs and the spacecraft measurement dis-
 628 agree in this region. The reason of this deviation must be the missing coupled in-

629 inner magnetosphere model. The applied tilted dipole approach is not satisfactory
 630 in the magnetosphere at all.

- 631 4. Disagreement between GUMICS–4 and observations does not seem to be due to
 632 **any particular** upstream solar wind **conditions**.
- 633 5. The position of the bow shock and the neutral sheet agrees well in the simulations
 634 and the Cluster SC3 magnetic field, ion plasma moments and derived electron den-
 635 sity measurements in this study. The position of the magnetopause does not fit
 636 that well.

637 The GUMICS–4 has scientific and strategic importance for the European Space Weather
 638 and Scientific community. This code developed in the Finnish Meteorological Institute
 639 is the most developed and tested, widely used tool for modelling the cosmic environment
 640 of the Earth in [...] Europe. An inner magnetosphere model should be two way cou-
 641 pled to the existing configuration of the simulation tool to improve the accuracy of the
 642 simulations.

643 Acknowledgments

644 The OMNI data were obtained from the GSFC/SPDF OMNIWeb interface at <http://omniweb.gsfc.nasa.gov>.
 645 The authors thank the FGM Team (PI: Chris Carr), the CIS Team (PI: Iannis Dandouras),
 646 the WHISPER Team (PI: Jean-Louis Rauch), the EFW Team (PI: Mats Andre) and the
 647 Cluster Science Archive for providing FGM magnetic field, CIS HIA ion plasma and WHIS-
 648 PER electron density measurements. Data analysis was partly done with the QSAS sci-
 649 ence analysis system provided by the United Kingdom Cluster Science Centre (Impe-
 650 rial College London and Queen Mary, University of London) supported by the Science
 651 and Technology Facilities Council (STFC). Eija Tanskanen acknowledges financial sup-
 652 port from the Academy of Finland for the ReSoLVE Centre of Excellence (project No. 272157).
 653 Gábor Facskó thanks Anna-Mária Vígh for improving the English of the paper. The au-
 654 thors thank Pekka Janhunen for developing the GUMICS–4 code; furthermore Minna
 655 Palmroth and Zoltán Vörös for the useful discussions. The work of Gábor Facskó was
 656 supported by mission science funding for the Van Allen Probes mission, the American
 657 Geophysical Union and the **Institute of Earth Physics and Space** Science, Sopron,
 658 Hungary. For further use of the year run data, request the authors or use the archive of
 659 the Community Coordinated Modelling Center (https://ccmc.gsfc.nasa.gov/publications/posted_runs/FacskoEA20)

660

661 References

- 662 Balogh, A., M. W. Dunlop, S. W. H. Cowley, D. J. Southwood, J. G. Thomlinson,
 663 K. H. Glassmeier, G. Musmann, H. Luhr, S. Buchert, M. H. Acuna, D. H. Fair-
 664 field, J. A. Slavin, W. Riedler, K. Schwingenschuh, and M. G. Kivelson (1997),
 665 The Cluster Magnetic Field Investigation, *Space Science Reviews*, 79, 65–91, doi:
 666 10.1023/A:1004970907748.
- 667 Balogh, A., C. M. Carr, M. H. Acuña, M. W. Dunlop, T. J. Beek, P. Brown,
 668 K. Fornaçon, E. Georgescu, K. Glassmeier, J. Harris, G. Musmann, T. Oddy, and
 669 K. Schwingenschuh (2001), The Cluster Magnetic Field Investigation: overview of
 670 in-flight performance and initial results, *Annales Geophysicae*, 19, 1207–1217.
- 671 Bartels, J., N. H. Heck, and H. F. Johnston (1939), The three-hour-range index mea-
 672 suring geomagnetic activity, *Terrestrial Magnetism and Atmospheric Electricity*
 673 (*Journal of Geophysical Research*), 44, 411, doi:10.1029/TE044i004p00411.
- 674 Blagau, A., I. Dandouras, A. Barthe, S. Brunato, G. Facskó, and V. Constanti-
 675 nescu (2013), In-flight calibration of Hot Ion Analyser onboard Cluster, *Geo-*
 676 *scientific Instrumentation, Methods and Data Systems Discussions*, 3, 407–435,
 677 doi:10.5194/gid-3-407-2013.
- 678 Blagau, A., I. Dandouras, A. Barthe, S. Brunato, G. Facskó, and V. Constantinescu
 679 (2014), In-flight calibration of the Hot Ion Analyser on board Cluster, *Geoscientific*
 680 *Instrumentation, Methods and Data Systems*, 3, 49–58, doi:10.5194/gi-3-49-
 681 2014.
- 682 Chittenden, J. P., S. V. Lebedev, C. A. Jennings, S. N. Bland , and A. Ciardi
 683 (2004), X-ray generation mechanisms in three-dimensional simulations of wire
 684 array Z-pinches, *Plasma Physics and Controlled Fusion*, 46(12B), B457–B476,
 685 doi:10.1088/0741-3335/46/12B/039.
- 686 Ciardi, A., S. V. Lebedev, A. Frank, E. G. Blackman, J. P. Chittenden, C. J. Jen-
 687 nings, D. J. Ampleford, S. N. Bland, S. C. Bott, J. Rapley, G. N. Hall, F. A.
 688 Suzuki-Vidal, A. Marocchino, T. Lery, and C. Stehle (2007), The evolution of
 689 magnetic tower jets in the laboratory, *Physics of Plasmas*, 14(5), 056,501–056,501,
 690 doi:10.1063/1.2436479.
- 691 Credland, J., G. Mecke, and J. Ellwood (1997), The Cluster Mission: ESA'S
 692 Spacefleet to the Magnetosphere, *Space Science Reviews*, 79, 33–64, doi:
 693 10.1023/A:1004914822769.

- 694 Davis, T. N., and M. Sugiura (1966), Auroral electrojet activity index AE and its
695 universal time variations, *Journal of Geophysical Research*, *71*, 785–801, doi:
696 10.1029/JZ071i003p00785.
- 697 Décréau, P. M. E., P. Fergeau, V. Krasnoselskikh, E. Le Guiriec, M. Lévéque,
698 P. Martin, O. Randriamboarison, J. L. Rauch, F. X. Sené, H. C. Séran, J. G.
699 Trotignon, P. Canu, N. Cornilleau, H. de Féraudy, H. Alleyne, K. Yearby, P. B.
700 Mögensen, G. Gustafsson, M. André, D. C. Gurnett, F. Darrouzet, J. Lemaire,
701 C. C. Harvey, P. Travnicek, and Whisper Experimenters Group (2001), Early re-
702 sults from the Whisper instrument on Cluster: an overview, *Annales Geophysicae*,
703 *19*, 1241–1258, doi:10.5194/angeo-19-1241-2001.
- 704 Escoubet, C. P., M. Fehringer, and M. Goldstein (2001), Introduction The Cluster
705 mission, *Annales Geophysicae*, *19*, 1197–1200, doi:10.5194/angeo-19-1197-2001.
- 706 Facskó, G., I. Honkonen, T. Živković, L. Palin, E. Kallio, K. Ågren, H. Opgenoorth,
707 E. I. Tanskanen, and S. Milan (2016), One year in the Earth's magnetosphere: A
708 global MHD simulation and spacecraft measurements, *Space Weather*, *14*, 351–
709 367, doi:10.1002/2015SW001355.
- 710 Facskó, G., T. B. Balogh, E. I. Anekallu, C. R. and Tanskanen, P. Peitso, L. Degener,
711 M. Kangwa, T. Laitinen, and S. Laakso, H. Burley (in preparation), Bow shock
712 identification in cluster measurements, *Space Weather*.
- 713 Fazakerley, A. N., A. D. Lahiff, R. J. Wilson, I. Rozum, C. Anekallu, M. West, and
714 H. Bacai (2010a), PEACE Data in the Cluster Active Archive, *Astrophysics and
715 Space Science Proceedings*, *11*, 129–144, doi:10.1007/978-90-481-3499-1_8.
- 716 Fazakerley, A. N., A. D. Lahiff, I. Rozum, D. Kataria, H. Bacai, C. Anekallu,
717 M. West, and A. Åsnes (2010b), Cluster-PEACE In-flight Calibration Status,
718 *Astrophysics and Space Science Proceedings*, *11*, 281–299, doi:10.1007/978-90-481-
719 3499-1_19.
- 720 García, K. S., and W. J. Hughes (2007), Finding the Lyon-Fedder-Mobarry mag-
721 netopause: A statistical perspective, *Journal of Geophysical Research (Space
722 Physics)*, *112*(A6), A06229, doi:10.1029/2006JA012039.
- 723 Gordeev, E., G. Facskó, V. Sergeev, I. Honkonen, M. Palmroth, P. Janhunen, and
724 S. Milan (2013), Verification of the GUMICS-4 global MHD code using empirical
725 relationships, *Journal of Geophysical Research (Space Physics)*, *118*, 3138–3146,
726 doi:10.1002/jgra.50359.

- 727 Greenwald, R. A., K. B. Baker, J. R. Dudeney, M. Pinnock, T. B. Jones, E. C.
728 Thomas, J.-P. Villain, J.-C. Cerisier, C. Senior, C. Hanuise, R. D. Hunsucker,
729 G. Sofko, J. Koehler, E. Nielsen, R. Pellinen, A. D. M. Walker, N. Sato,
730 and H. Yamagishi (1995), Darn/Superdarn: A Global View of the Dynam-
731 ics of High-Latitude Convection, *Space Science Reviews*, *71*, 761–796, doi:
732 10.1007/BF00751350.
- 733 Guild, T. B., H. E. Spence, E. L. Kepko, V. Merkin, J. G. Lyon, M. Wiltberger, and
734 C. C. Goodrich (2008a), Geotail and LFM comparisons of plasma sheet clima-
735 tology: 1. Average values, *Journal of Geophysical Research (Space Physics)*, *113*,
736 A04216, doi:10.1029/2007JA012611.
- 737 Guild, T. B., H. E. Spence, E. L. Kepko, V. Merkin, J. G. Lyon, M. Wiltberger, and
738 C. C. Goodrich (2008b), Geotail and LFM comparisons of plasma sheet climatol-
739 ogy: 2. Flow variability, *Journal of Geophysical Research (Space Physics)*, *113*,
740 A04217, doi:10.1029/2007JA012613.
- 741 Gustafsson, G., R. Bostrom, B. Holback, G. Holmgren, A. Lundgren, K. Stasiewicz,
742 L. Ahlen, F. S. Mozer, D. Pankow, P. Harvey, P. Berg, R. Ulrich, A. Pedersen,
743 R. Schmidt, A. Butler, A. W. C. Fransen, D. Klinge, M. Thomsen, C.-G. Faltham-
744 mar, P.-A. Lindqvist, S. Christenson, J. Holtet, B. Lybekk, T. A. Sten, P. Tan-
745 skanen, K. Lappalainen, and J. Wygant (1997), The Electric Field and Wave
746 Experiment for the Cluster Mission, *Space Science Reviews*, *79*, 137–156, doi:
747 10.1023/A:1004975108657.
- 748 Gustafsson, G., M. André, T. Carozzi, A. I. Eriksson, C.-G. Fälthammar, R. Grard,
749 G. Holmgren, J. A. Holtet, N. Ivchenko, T. Karlsson, Y. Khotyaintsev, S. Klimov,
750 H. Laakso, P.-A. Lindqvist, B. Lybekk, G. Marklund, F. Mozer, K. Mursula,
751 A. Pedersen, B. Popielawska, S. Savin, K. Stasiewicz, P. Tanskanen, A. Vaivads,
752 and J.-E. Wahlund (2001), First results of electric field and density observations
753 by Cluster EFW based on initial months of operation, *Annales Geophysicae*, *19*,
754 1219–1240, doi:10.5194/angeo-19-1219-2001.
- 755 Haiducek, J. D., D. T. Welling, N. Y. Ganushkina, S. K. Morley, and D. S. Oz-
756 turk (2017), SWMF Global Magnetosphere Simulations of January 2005: Geo-
757 magnetic Indices and Cross-Polar Cap Potential, *Space Weather*, *15*, 1567–1587,
758 doi:10.1002/2017SW001695.
- 759 Iyemori, T. (1990), Storm-time magnetospheric currents inferred from mid-latitude

- 760 geomagnetic field variations, *Journal of Geomagnetism and Geoelectricity*, 42,
761 1249–1265, doi:10.5636/jgg.42.1249.
- 762 Janhunen, P., M. Palmroth, T. Laitinen, I. Honkonen, L. Juusola, G. Facskó, and
763 T. I. Pulkkinen (2012), The GUMICS-4 global MHD magnetosphere-ionosphere
764 coupling simulation, *Journal of Atmospheric and Solar-Terrestrial Physics*, 80,
765 48–59, doi:10.1016/j.jastp.2012.03.006.
- 766 Johnstone, A. D., C. Alsop, S. Burge, P. J. Carter, A. J. Coates, A. J. Coker, A. N.
767 Fazakerley, M. Grande, R. A. Gowen, C. Gurgiolo, B. K. Hancock, B. Narheim,
768 A. Preece, P. H. Sheather, J. D. Winningham, and R. D. Woodliffe (1997), Peace:
769 a Plasma Electron and Current Experiment, *Space Science Reviews*, 79, 351–398,
770 doi:10.1023/A:1004938001388.
- 771 Juusola, L., O. Amm, K. Kauristie, and A. Viljanen (2007), A model for estimating
772 the relation between the Hall to Pedersen conductance ratio and ground magnetic
773 data derived from CHAMP satellite statistics, *Annales Geophysicae*, 25, 721–736,
774 doi:10.5194/angeo-25-721-2007.
- 775 Juusola, L., G. Facskó, I. Honkonen, P. Janhunen, H. Vanhamäki, K. Kauristie,
776 T. V. Laitinen, S. E. Milan, M. Palmroth, E. I. Tanskanen, and A. Viljanen
777 (2014), Statistical comparison of seasonal variations in the GUMICS-4 global
778 MHD model ionosphere and measurements, *Space Weather*, 12, 582–600, doi:
779 10.1002/2014SW001082.
- 780 Kallio, E., and G. Facskó (2015), Properties of plasma near the moon in the magne-
781 totail, *Planetary and Space Science*, 115, 69–76, doi:10.1016/j.pss.2014.11.007.
- 782 Kokubun, S., T. Yamamoto, M. H. Acuña, K. Hayashi, K. Shiokawa, and H. Kawano
783 (1994), The GEOTAIL Magnetic Field Experiment., *Journal of Geomagnetism*
784 and *Geoelectricity*, 46, 7–21, doi:10.5636/jgg.46.7.
- 785 Lakka, A., T. I. Pulkkinen, A. P. Dimmock, M. Myllys, I. Honkonen, and M. Palm-
786 roth (2018a), The Cross-Polar Cap Saturation in GUMICS-4 During High Solar
787 Wind Driving, *Journal of Geophysical Research (Space Physics)*, 123, 3320–3332,
788 doi:10.1002/2017JA025054.
- 789 Lakka, A., T. I. Pulkkinen, A. P. Dimmock, E. Kilpua, M. Ala-Lahti, I. Honko-
790 nen, M. Palmroth, and Raukunen (2018b), Icme impact at earth with low and
791 typical mach number plasma characteristics, *Annales Geophysicae Discussions*,
792 <https://doi.org/10.5194/angeo-2018-81>.

- 793 Lani, A., A. Sanna, N. Villedieu, and M. Panesi (2012), COOLFluiD an Open Com-
794 putational Platform for Aerothermodynamics and Flow-Radiation Coupling, in
795 *ESA Special Publication, ESA Special Publication*, vol. 714, p. 45.
- 796 Liemohn, M., N. Y. Ganushkina, D. L. De Zeeuw, L. Rastaetter, M. Kuznetsova,
797 D. T. Welling, G. Toth, R. Ilie, T. I. Gombosi, and B. van der Holst (2018), Real-
798 Time SWMF at CCMC: Assessing the Dst Output From Continuous Operational
799 Simulations, *Space Weather*, 16(10), 1583–1603, doi:10.1029/2018SW001953.
- 800 Lyon, J. G., J. A. Fedder, and C. M. Mobarry (2004), The Lyon-Fedder-Mobarry
801 (LFM) global MHD magnetospheric simulation code, *Journal of Atmospheric and*
802 *Solar-Terrestrial Physics*, 66, 1333–1350, doi:10.1016/j.jastp.2004.03.020.
- 803 Mejnertsen, L., J. P. Eastwood, J. P. Chittenden, and A. Masters (2016), Global
804 MHD simulations of Neptune’s magnetosphere, *Journal of Geophysical Research*
805 (*Space Physics*), 121(8), 7497–7513, doi:10.1002/2015JA022272.
- 806 Mejnertsen, L., J. P. Eastwood, H. Hietala, S. J. Schwartz, and J. P. Chittenden
807 (2018), Global MHD Simulations of the Earth’s Bow Shock Shape and Motion
808 Under Variable Solar Wind Conditions, *Journal of Geophysical Research (Space*
809 *Physics*), 123(1), 259–271, doi:10.1002/2017JA024690.
- 810 Mukai, T., S. Machida, Y. Saito, M. Hirahara, T. Terasawa, N. Kaya, T. Obara,
811 M. Ejiri, and A. Nishida (1994), The Low Energy Particle (LEP) Experiment on-
812 board the GEOTAIL Satellite., *Journal of Geomagnetism and Geoelectricity*, 46,
813 669–692, doi:10.5636/jgg.46.669.
- 814 Peredo, M., J. A. Slavin, E. Mazur, and S. A. Curtis (1995), Three-dimensional po-
815 sition and shape of the bow shock and their variation with Alfvénic, sonic and
816 magnetosonic Mach numbers and interplanetary magnetic field orientation, *Jour-*
817 *nal of Geophysical Research*, 100, 7907–7916, doi:10.1029/94JA02545.
- 818 Poedts, S., A. Kochanov, A. Lani, C. Scolini, C. Verbeke, S. Hosteaux, E. Chané,
819 H. Deconinck, N. Mihalache, F. Diet, D. Heynderickx, J. De Keyser, E. De
820 Donder, N. B. Crosby, M. Echim, L. Rodriguez, R. Vansintjan, F. Verstringe,
821 B. Mampaey, R. Horne, S. Glauert, P. Jiggens, R. Keil, A. Glover, G. Deprez, and
822 J.-P. Luntama (2020), The Virtual Space Weather Modelling Centre, *Journal of*
823 *Space Weather and Space Climate*, 10, 14, doi:10.1051/swsc/2020012.
- 824 Powell, K. G., P. L. Roe, T. J. Linde, T. I. Gombosi, and D. L. De Zeeuw (1999), A
825 Solution-Adaptive Upwind Scheme for Ideal Magnetohydrodynamics, *Journal of*

- 826 *Computational Physics*, *154*, 284–309, doi:10.1006/jcph.1999.6299.
- 827 Raeder, J., D. Larson, W. Li, E. L. Kepko, and T. Fuller-Rowell (2008), OpenG-
828 GCM Simulations for the THEMIS Mission, *Space Science Reviews*, *141*, 535–555,
829 doi:10.1007/s11214-008-9421-5.
- 830 Reigber, C., H. Lühr, and P. Schwintzer (2002), CHAMP mission status, *Advances
831 in Space Research*, *30*, 129–134, doi:10.1016/S0273-1177(02)00276-4.
- 832 Reme, H., J. M. Bosqued, J. A. Sauvaud, A. Cros, J. Dandouras, C. Aoustin,
833 J. Bouyssou, T. Camus, J. Cuvilo, C. Martz, J. L. Medale, H. Perrier, D. Rome-
834 fort, J. Rouzaud, C. D'Uston, E. Möbius, K. Crocker, M. Granoff, L. M. Kistler,
835 M. Popecki, D. Hovestadt, B. Klecker, G. Paschmann, M. Scholer, C. W. Carl-
836 son, D. W. Curtis, R. P. Lin, J. P. McFadden, V. Formisano, E. Amata, M. B.
837 Bavassano-Cattaneo, P. Baldetti, G. Belluci, R. Bruno, G. Chionchio, A. di Lel-
838 lis, E. G. Shelley, A. G. Ghielmetti, W. Lennartsson, A. Korth, H. Rosenbauer,
839 R. Lundin, S. Olsen, G. K. Parks, M. McCarthy, and H. Balsiger (1997), The
840 Cluster Ion Spectrometry (CIS) Experiment, *Space Science Reviews*, *79*, 303–350,
841 doi:10.1023/A:1004929816409.
- 842 Rème, H., C. Aoustin, J. M. Bosqued, I. Dandouras, B. Lavraud, J. A. Sauvaud,
843 A. Barthe, J. Bouyssou, T. Camus, O. Coeur-Joly, A. Cros, J. Cuvilo, F. Ducay,
844 Y. Garbarowitz, J. L. Medale, E. Penou, H. Perrier, D. Romefort, J. Rouzaud,
845 C. Vallat, D. Alcaydé, C. Jacquey, C. Mazelle, C. D'Uston, E. Möbius, L. M.
846 Kistler, K. Crocker, M. Granoff, C. Mouikis, M. Popecki, M. Vosbury, B. Klecker,
847 D. Hovestadt, H. Kucharek, E. Kuenneth, G. Paschmann, M. Scholer, N. Sckopke,
848 E. Seidenschwang, C. W. Carlson, D. W. Curtis, C. Ingraham, R. P. Lin, J. P.
849 McFadden, G. K. Parks, T. Phan, V. Formisano, E. Amata, M. B. Bavassano-
850 Cattaneo, P. Baldetti, R. Bruno, G. Chionchio, A. di Lellis, M. F. Marcucci,
851 G. Pallocchia, A. Korth, P. W. Daly, B. Graeve, H. Rosenbauer, V. Vasyliunas,
852 M. McCarthy, M. Wilber, L. Eliasson, R. Lundin, S. Olsen, E. G. Shelley, S. Fusse-
853 lier, A. G. Ghielmetti, W. Lennartsson, C. P. Escoubet, H. Balsiger, R. Friedel, J.-
854 B. Cao, R. A. Kovarazhkin, I. Papamastorakis, R. Pellat, J. Scudder, and B. Son-
855 nerup (2001), First multispacecraft ion measurements in and near the Earth's
856 magnetosphere with the identical Cluster ion spectrometry (CIS) experiment,
857 *Annales Geophysicae*, *19*, 1303–1354, doi:10.5194/angeo-19-1303-2001.
- 858 Ritter, P., H. Lühr, A. Viljanen, O. Amm, A. Pulkkinen, and I. Sillanpää (2004),

- 859 Ionospheric currents estimated simultaneously from CHAMP satellite and IMAGE
 860 ground-based magnetic field measurements: a statistical study at auroral latitudes,
 861 *Annales Geophysicae*, 22, 417–430, doi:10.5194/angeo-22-417-2004.
- 862 Rostoker, G. (1972), Geomagnetic indices., *Reviews of Geophysics and Space*
 863 *Physics*, 10, 935–950, doi:10.1029/RG010i004p00935.
- 864 Siscoe, G. L., G. M. Erickson, B. U. Sonnerup, N. C. Maynard, J. A. Schoendorf,
 865 K. D. Siebert, D. R. Weimer, W. W. White, and G. R. Wilson (2001), The Mag-
 866 netospheric Fluopause, in *AGU Spring Meeting Abstracts*, vol. 2001, pp. SM52D–
 867 02.
- 868 Sofko, G. J., R. Greenwald, and W. Bristow (1995), Direct determination of large-
 869 scale magnetospheric field-aligned currents with SuperDARN, *Geophysical Re-*
 870 *search Letters*, 22, 2041–2044, doi:10.1029/95GL01317.
- 871 Thomsen, M. F. (2004), Why K_p is such a good measure of magnetospheric convec-
 872 tion, *Space Weather*, 2, S11004, doi:10.1029/2004SW000089.
- 873 Tóth, G., I. V. Sokolov, T. I. Gombosi, D. R. Chesney, C. R. Clauer, D. L. de
 874 Zeeuw, K. C. Hansen, K. J. Kane, W. B. Manchester, R. C. Oehmke, K. G. Pow-
 875 ell, A. J. Ridley, I. I. Roussev, Q. F. Stout, O. Volberg, R. A. Wolf, S. Sazykin,
 876 A. Chan, B. Yu, and J. Kóta (2005), Space Weather Modeling Framework: A
 877 new tool for the space science community, *Journal of Geophysical Research (Space*
 878 *Physics)*, 110, A12226, doi:10.1029/2005JA011126.
- 879 Tóth, G., B. van der Holst, I. V. Sokolov, D. L. De Zeeuw, T. I. Gombosi, F. Fang,
 880 W. B. Manchester, X. Meng, D. Najib, K. G. Powell, Q. F. Stout, A. Glo-
 881 cer, Y.-J. Ma, and M. Opher (2012), Adaptive numerical algorithms in space
 882 weather modeling, *Journal of Computational Physics*, 231, 870–903, doi:
 883 10.1016/j.jcp.2011.02.006.
- 884 Trotignon, J. G., P. M. E. Décréau, J. L. Rauch, X. Vallières, A. Rochel,
 885 S. Kougblénou, G. Lointier, G. Facskó, P. Canu, F. Darrouzet, and A. Masson
 886 (2010), The WHISPER Relaxation Sounder and the CLUSTER Active Archive,
 887 *Astrophysics and Space Science Proceedings*, 11, 185–208, doi:10.1007/978-90-481-
 888 3499-1_12.
- 889 Trotignon, J.-G., Vallières, and the WHISPER team (2011), Calibration report of
 890 the whisper measurements in the cluster active archive (caa), *Tech. rep.*, LPC2E
 891 CNRS, caa-est-cr-whi.

- 892 Tsyganenko, N. A. (1995), Modeling the Earth's magnetospheric magnetic field
893 confined within a realistic magnetopause, *Journal of Geophysical Research*, 100,
894 5599–5612, doi:10.1029/94JA03193.
- 895 Vörös, Z., G. Facskó, M. Khodachenko, I. Honkonen, P. Janhunen, and M. Palmroth
896 (2014), Windsock memory COnditioned RAM (CO-RAM) pressure effect: Forced
897 reconnection in the Earth's magnetotail, *Journal of Geophysical Research (Space*
898 *Physics)*, 119, 6273–6293, doi:10.1002/2014JA019857.
- 899 Wang, Z.-D., and R. L. Xu (1994), Signatures of the magnetotail neutral sheet,
900 *Geophysical Research Letters*, 21(19), 2087–2090, doi:10.1029/94GL01960.
- 901 Weimer, D. R. (2005), Improved ionospheric electrodynamic models and applica-
902 tion to calculating Joule heating rates, *Journal of Geophysical Research (Space*
903 *Physics)*, 110, A05306, doi:10.1029/2004JA010884.
- 904 Wiltberger, M., E. J. Rigler, V. Merkin, and J. G. Lyon (2017), Structure of High
905 Latitude Currents in Magnetosphere-Ionosphere Models, *Space Science Reviews*,
906 206, 575–598, doi:10.1007/s11214-016-0271-2.
- 907 Zhang, B., W. Lotko, M. J. Wiltberger, O. J. Brambles, and P. A. Damiano (2011),
908 A statistical study of magnetosphere-ionosphere coupling in the Lyon-Fedder-
909 Mobarry global MHD model, *Journal of Atmospheric and Solar-Terrestrial*
910 *Physics*, 73, 686–702, doi:10.1016/j.jastp.2010.09.027.
- 911 Zhang, B., K. A. Sorathia, J. G. Lyon, V. G. Merkin, J. S. Garretson, and M. Wilt-
912 berger (2019), GAMERA: A Three-dimensional Finite-volume MHD Solver for
913 Non-orthogonal Curvilinear Geometries, *The Astrophysical Journal Supplement*
914 *Series*, 244(1), 20, doi:10.3847/1538-4365/ab3a4c.

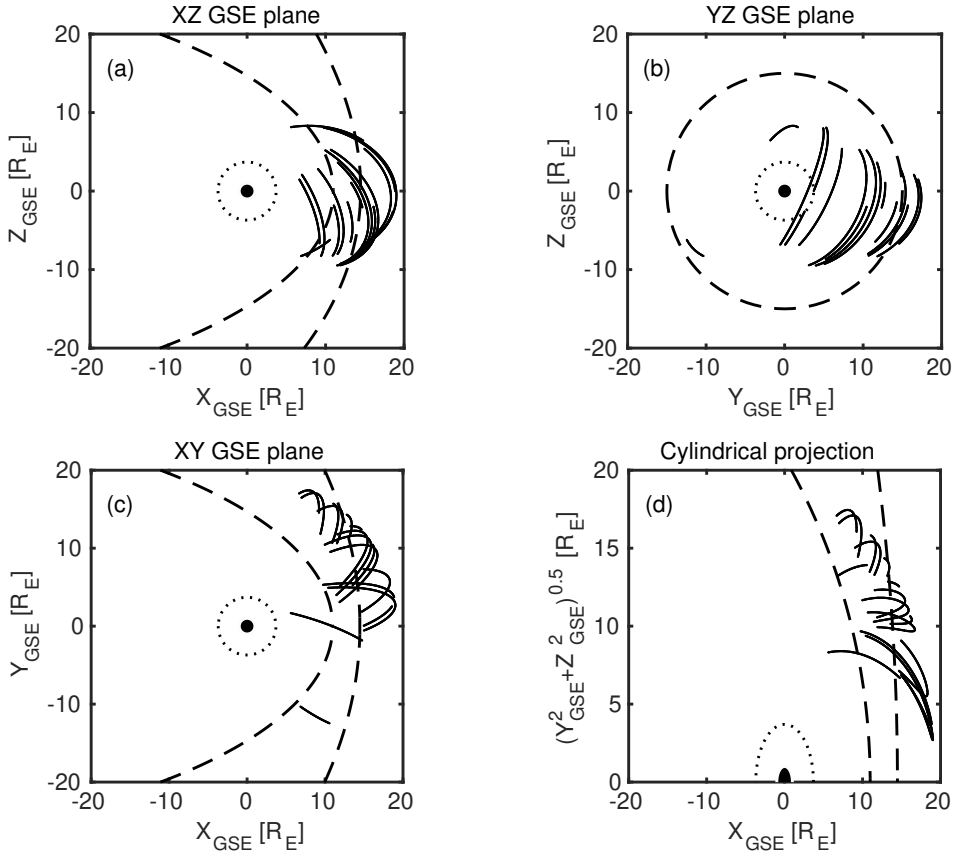


Figure 1. Cluster SC3 orbit in the solar wind in GSE system for all intervals (see Table 1).
 (a) XZ (b) YZ (c) XY (d) Cylindrical projection. Average bow-shock and magnetopause positions are drawn on all plots using dashed lines [Perego *et al.*, 1995; Tsyganenko, 1995, respectively]. The black dots at $3.7 R_E$ show the boundary of the GUMICS-4 inner magnetospheric domain. The black circle in the origo of all plots shows the size of the Earth.

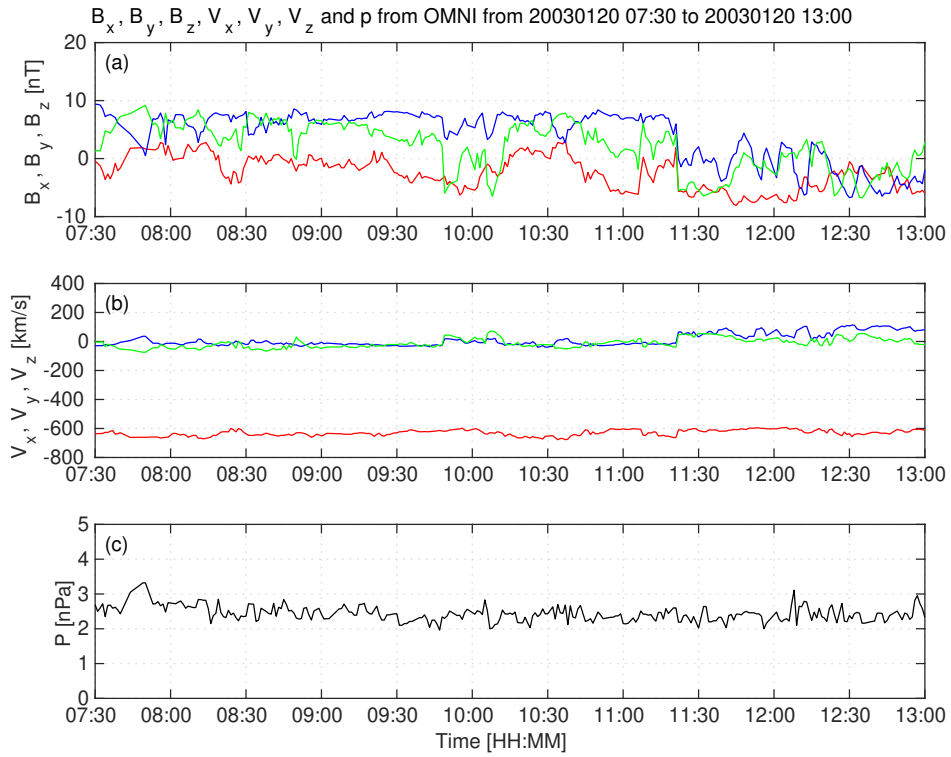
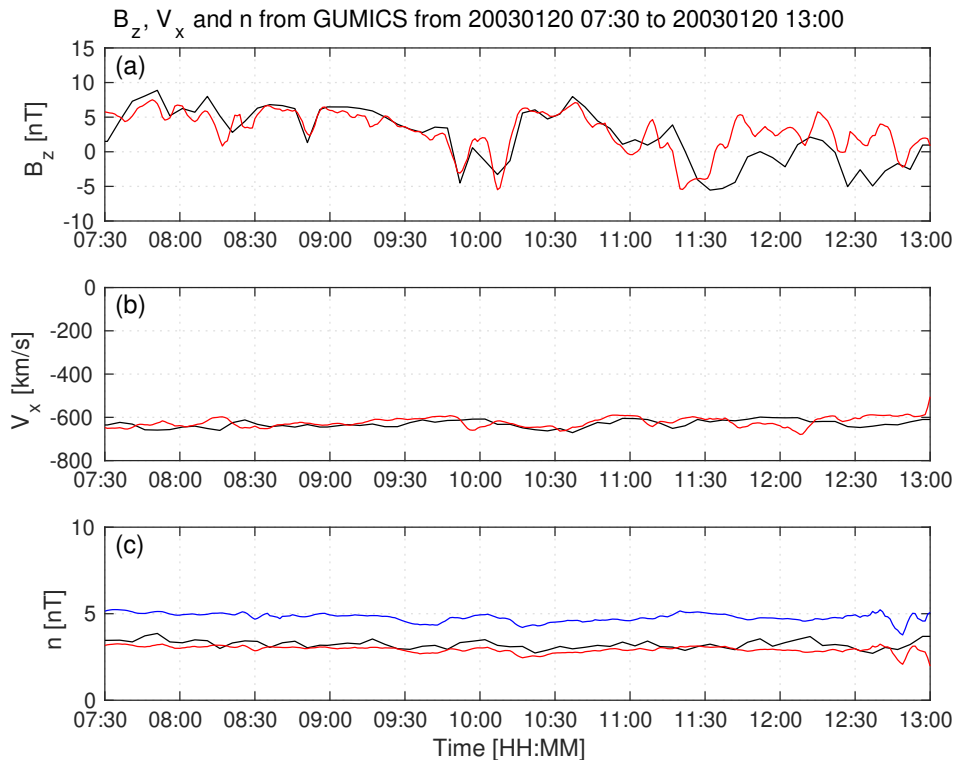
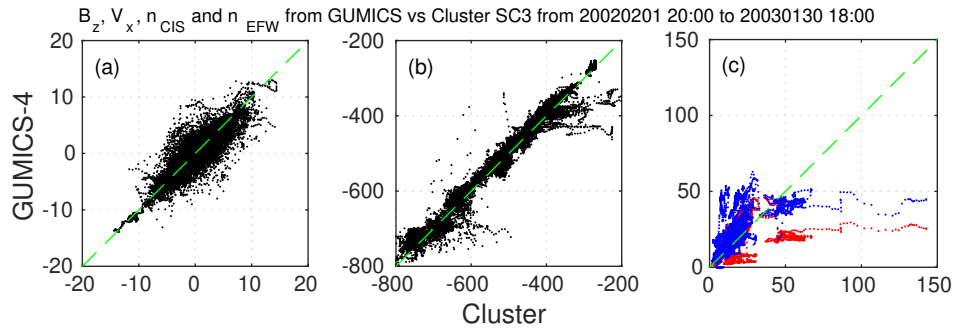


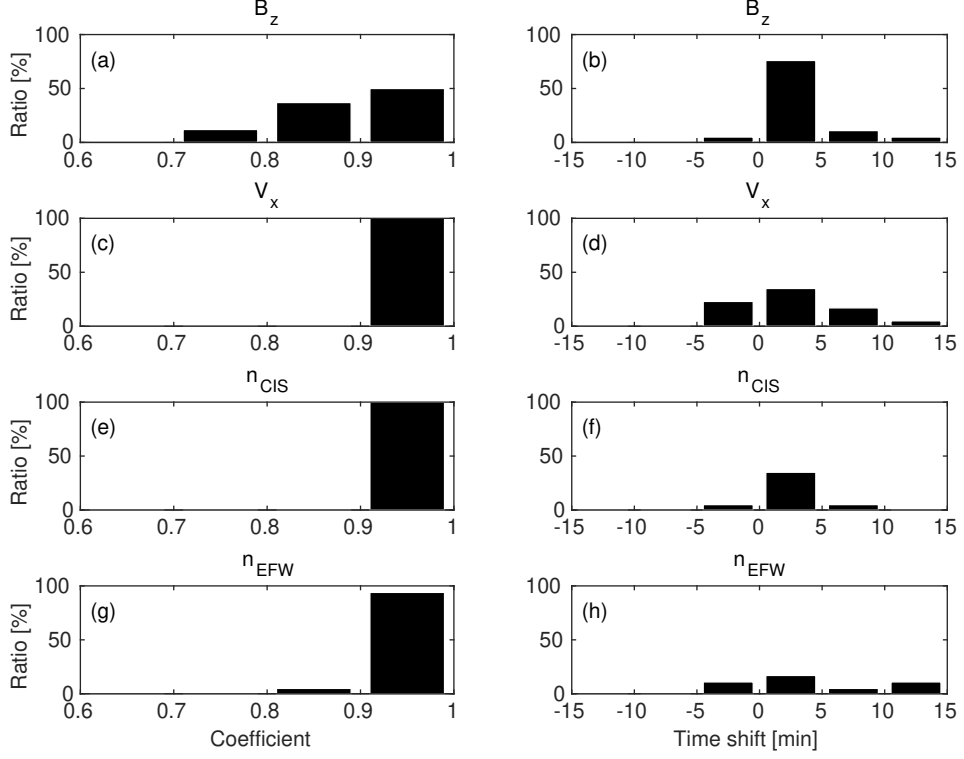
Figure 2. OMNI solar wind data in GSE system from 7:30 to 13:00 (UT) on January 20, 2003. (a) Magnetic field B_x (red), B_y (green) and B_z (blue) components. (b) Solar wind velocity V_x (red), V_y (green) and V_z (blue) components. (c) The P pressure of the solar wind (black).



923 **Figure 3.** GUMICS-4 simulation results (black) and Cluster SC3 magnetic field Z component,
924 ion plasma moments (red) and electron density calculated from spacecraft potential (blue) from
925 January 20, 2003 from 7:30 to 13:00 (UT) in the solar wind in GSE system. (a) Magnetic field Z
926 component. (b) Solar wind velocity X component (c) Solar wind density.



927 **Figure 4.** Scattered plots of the Cluster SC3 and GUMICS-4 simulations for all intervals in
928 the solar wind. The dashed line is the $y=x$ line. (a) Magnetic field Z component in GSE system.
929 (b) Solar wind velocity X component in GSE system. (c) Solar wind density measured by the
930 CIS HIA instrument (red) and calculated from the spacecraft potential (blue).



931 **Figure 5.** The distributions of the highest **cross-correlation coefficients** (a, c, e, g) of the
 932 magnetic field Z component (B_z) in GSE system, solar wind velocity X component (V_x) in GSE
 933 system, the solar wind density measured by the CIS HIA (n_{CIS}) instrument and calculated from
 934 the spacecraft potential (n_{EFW}), respectively, for all intervals in the solar wind. The distribu-
 935 tions of the corresponding time shifts (b, d, f, h) of the B_z , the V_x , the n_{CIS} and the n_{EFW}),
 936 respectively, for all intervals in the solar wind.

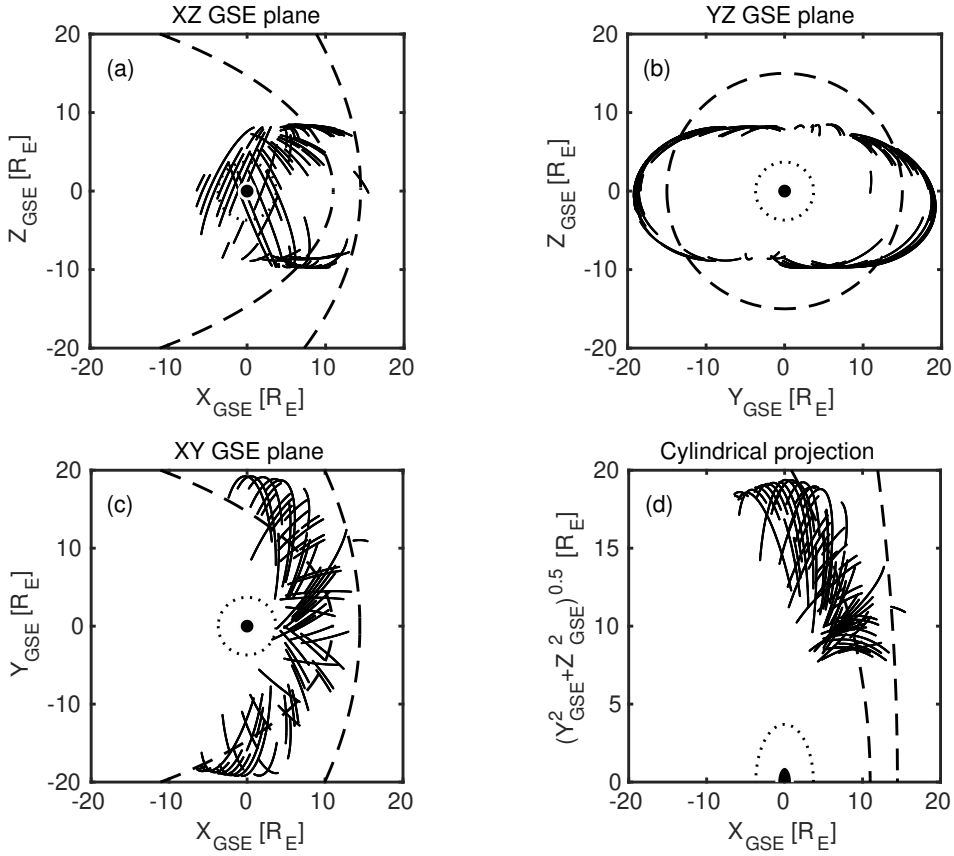
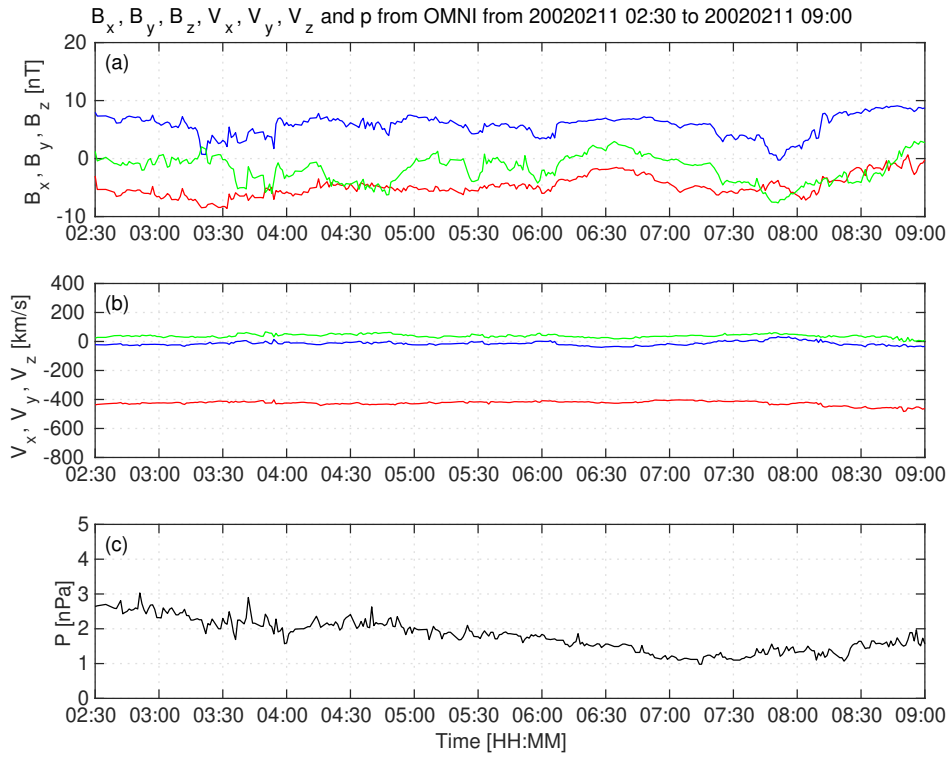
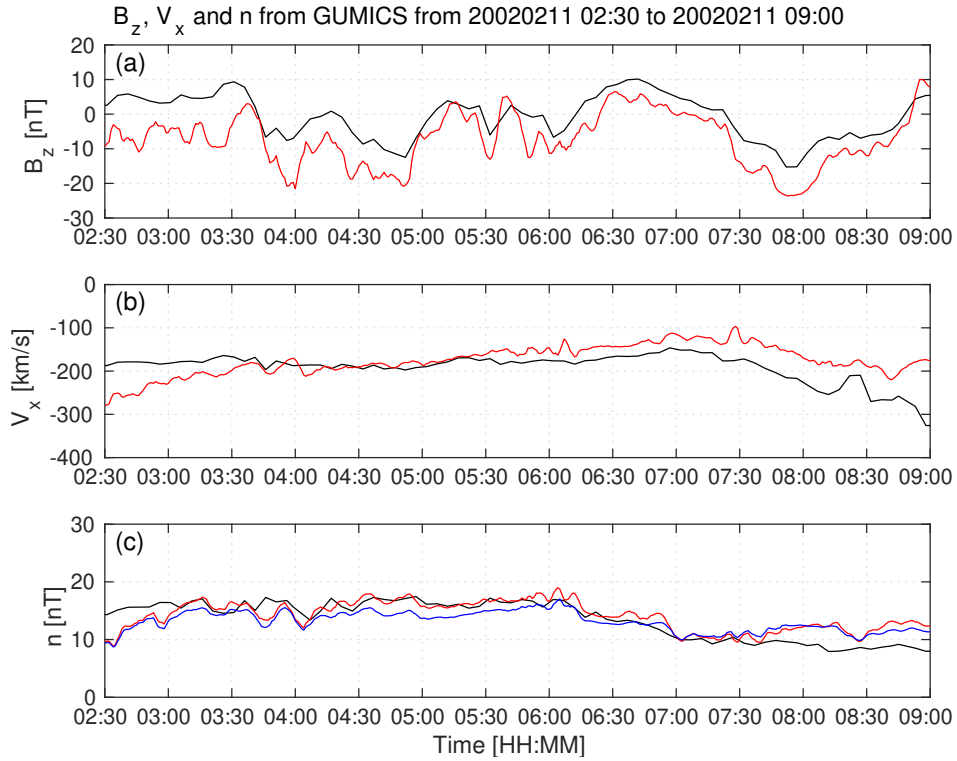


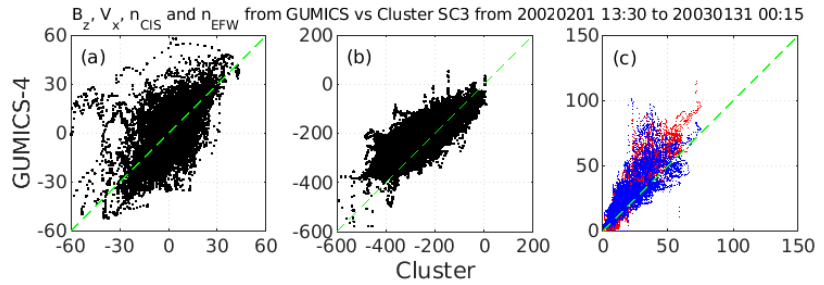
Figure 6. Cluster SC3 orbit in the magnetosheath in GSE system for all intervals (see Table 2). (a) XZ (b) YZ (c) XY (d) Cylindrical projection. Average bow-shock and magnetopause positions are drawn on all plots using dashed lines [Perego *et al.*, 1995; Tsyganenko, 1995, respectively]. The black dots at $3.7 R_E$ show the boundary of the GUMICS-4 inner magnetospheric domain. The black circle in the origo of all plots shows the size of the Earth.



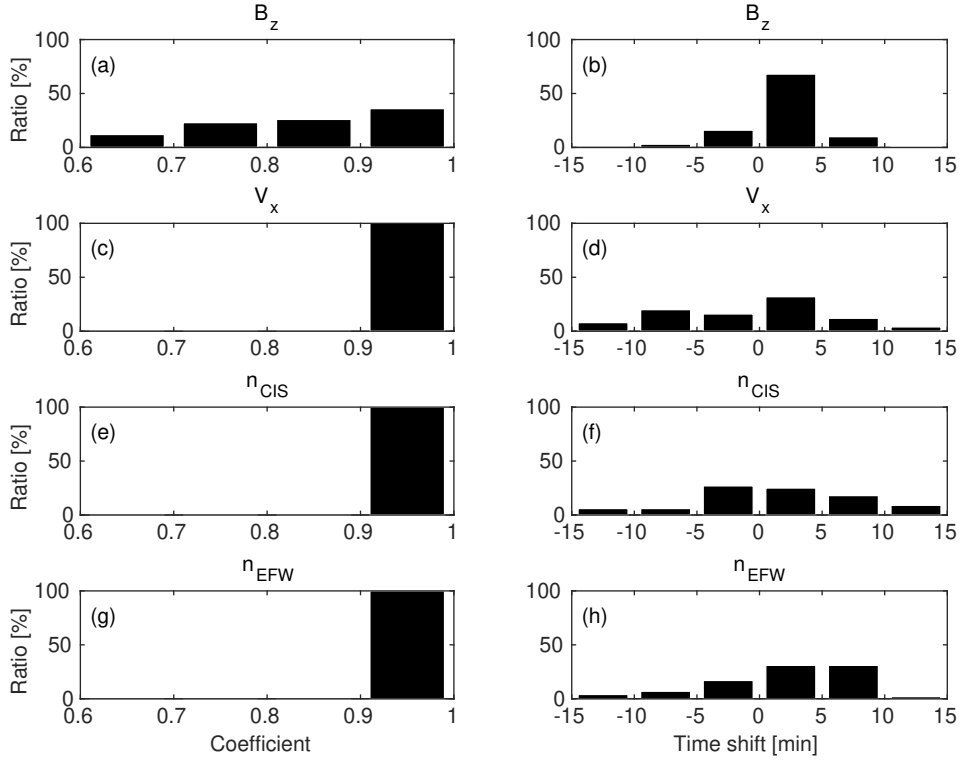
942 **Figure 7.** OMNI solar wind data in GSE system from 2:30 to 09:00 (UT) on February 11,
943 2002. (a) Magnetic field B_x (red), B_y (green) and B_z (blue) components. (b) Solar wind velocity
944 V_x (red), V_y (green) and V_z (blue) components. (c) The P pressure of the solar wind (black).



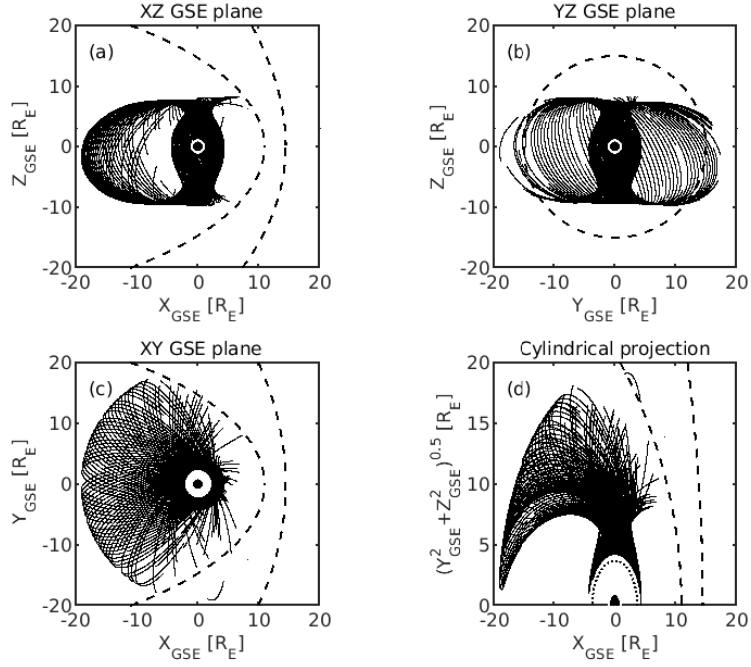
945 **Figure 8.** GUMICS-4 simulation results (black) and Cluster SC3 magnetic field Z component,
 946 ion plasma moments (red) and electron density calculated from spacecraft potential (blue) from
 947 February 11, 2002 from 2:30 to 9:00 (UT) in the magnetosheath in GSE system (a) Magnetic
 948 field Z component. (b) Solar wind velocity X component (c) Solar wind density.



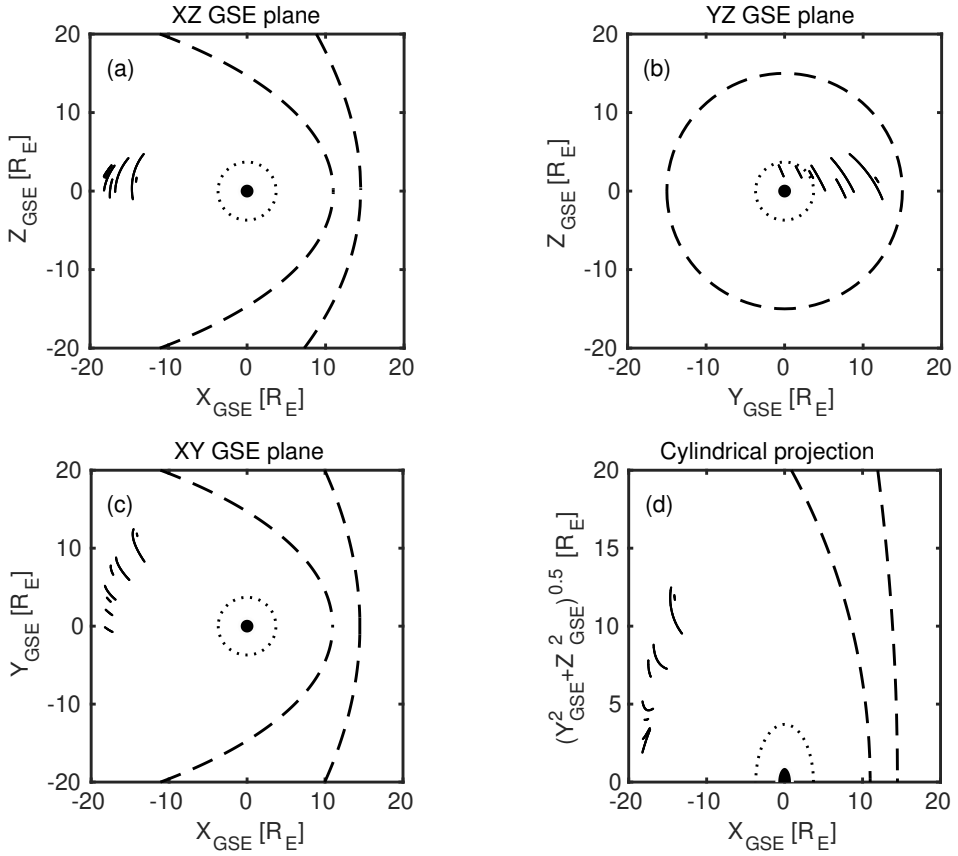
949 **Figure 9.** Scattered plots of the Cluster SC3 and GUMICS–4 simulations for all intervals in
 950 the magnetosheath in GSE system. The dashed line is the $y=x$ line. (a) Magnetic field Z com-
 951 ponent. (b) Solar wind velocity X component. (c) Solar wind density measured by the CIS HIA
 952 instrument (red) and calculated from the spacecraft potential (blue).



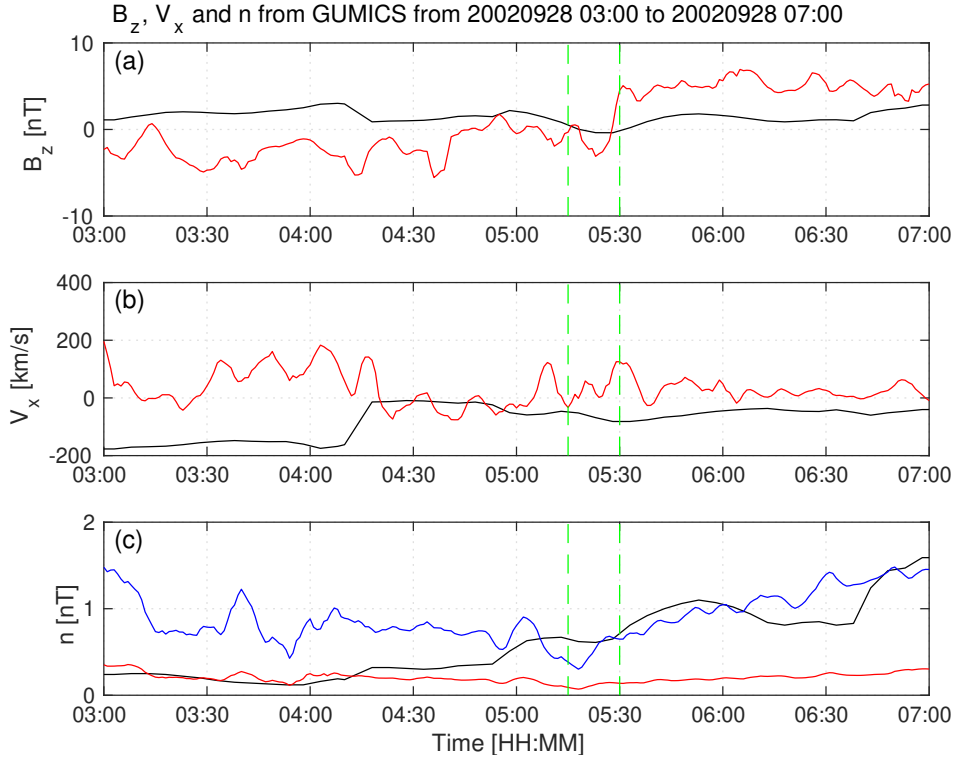
953 **Figure 10.** The distributions of the cross-correlation coefficients (a, c, e, g) of the magnetic
 954 field Z component (B_z) in GSE system, solar wind velocity X component (V_x) in GSE system,
 955 the solar wind density measured by the CIS HIA (n_{CIS}) instrument and calculated from the
 956 spacecraft potential (n_{EFW}), respectively, for all intervals in the magnetosheath. The distribu-
 957 tions of the time shifts (b, d, f, h) of the B_z , the V_x , the n_{CIS} and the n_{EFW}), respectively, for
 958 all intervals in the magnetosheath.



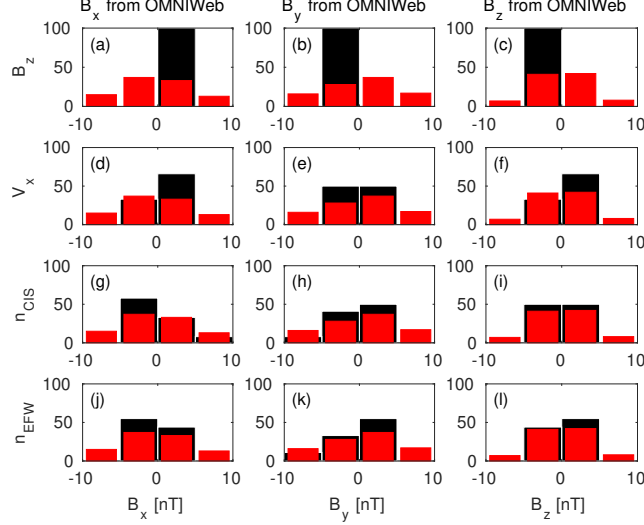
959 **Figure 11.** Cluster SC3 orbit in the magnetosphere in GSE system for all intervals (see Ta-
 960 ble 3). (a) XZ (b) YZ (c) XY (d) Cylindrical projection. Average bow-shock and magnetopause
 961 positions are drawn on all plots using dashed lines [Perego *et al.*, 1995; Tsyganenko, 1995, respec-
 962 tively]. The black dots at $3.7 R_E$ show the boundary of the GUMICS-4 inner magnetospheric
 963 domain. The black circle in the origo of all plots shows the size of the Earth.



964 **Figure 12.** Cluster SC3 orbit in the tail in GSE system for all intervals (see Table 6). (a) XZ
 965 (b) YZ (c) XY (d) Cylindrical projection. Average bow-shock and magnetopause positions are
 966 drawn on all plots using dashed lines [Peredo *et al.*, 1995; Tsyganenko, 1995, respectively]. The
 967 black dots at $3.7 R_E$ show the boundary of the GUMICS-4 inner magnetospheric domain. The
 968 black circle in the origo of all plots shows the size of the Earth.



969 **Figure 13.** GUMICS-4 simulation results (black) and Cluster SC3 magnetic field Z compo-
 970 nent, ion plasma moments (red) and electron density calculated from spacecraft potential (blue)
 971 from September 28, 2002 from 3:00 to 7:00 (UT) in the tail in GSE system. (a) Magnetic field
 972 Z component. (b) Solar wind velocity X component (c) Solar wind density. From 05:15 to 05:30
 973 between the green dashed vertical lines both the Cluster SC3 and the virtual spaceprobe of the
 974 GUMICS-4 simulation cross the neutral sheet multiple times.



975 **Figure 14.** The black distributions of the B_x , the B_y and the B_z OMNI solar wind magnetic
 976 field components when the agreement of the Cluster SC3 measurements and the GUMICS-4
 977 simulations are poor in the solar wind (see Table 7). The B_z , the V_x , the n_{CIS} and the n_{EFW}
 978 are the magnetic field GSE Z component, the plasma ion velocity X GSE component, the solar
 979 wind density measured by the CIS HIA instrument and the calculated from the EFW spacecraft
 980 potential, respectively. (a, b, c) Distribution of OMNI B_x , B_y , B_z when the agreement of B_z
 981 is poor. (d, e, f) Distribution of OMNI B_x , B_y , B_z when the agreement of V_x is poor. (g, h, i)
 982 Distribution of OMNI B_x , B_y , B_z when the agreement of n_{CIS} is poor. (j, k, l) Distribution of
 983 OMNI B_x , B_y , B_z when the agreement of n_{EFW} is poor. The values are in percentage units in
 984 the distributions. The red distributions of (a, d, g, j), (b, e, h, k) and (c, f, i, l) are the distribu-
 985 tion of the B_x , the B_y , and the B_z components of the OMNI solar wind magnetic field during the
 986 1-year run from January 29, 2002, to February 2, 2003, in GSE reference frame, respectively.

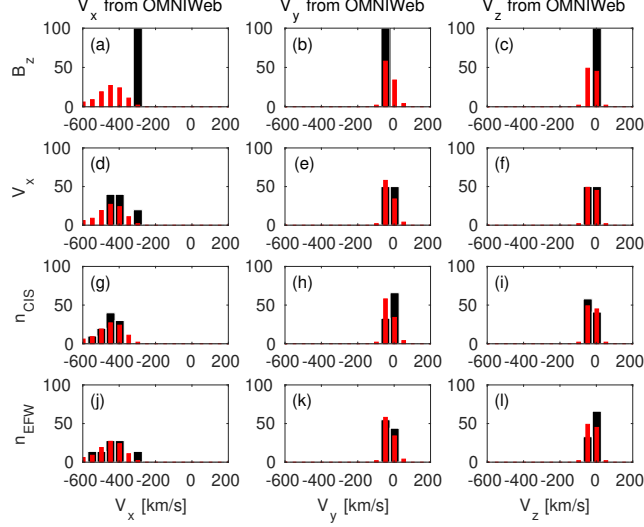
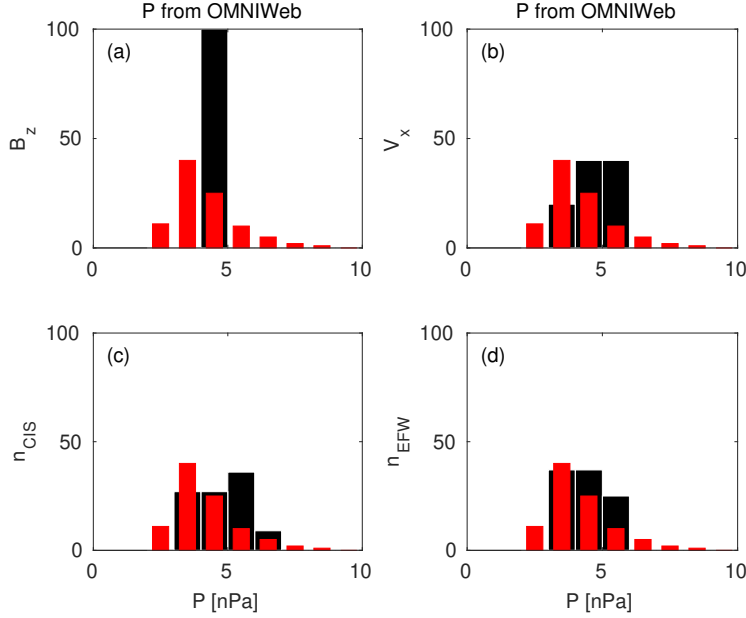
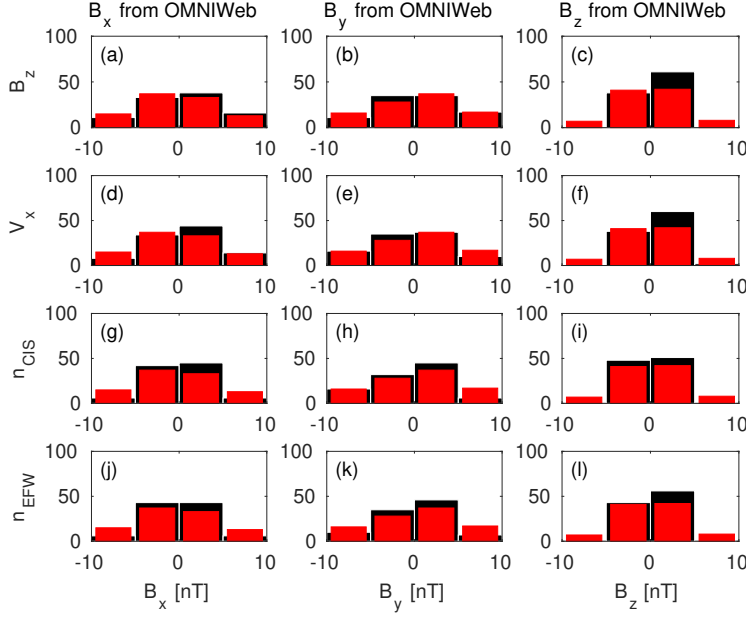


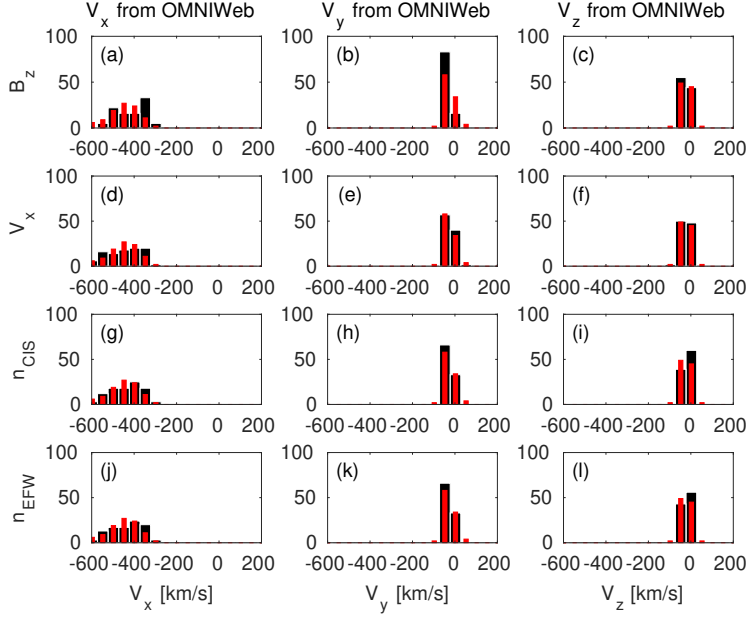
Figure 15. The black distributions of the V_x , the V_y and the V_z OMNI solar wind magnetic field components when the agreement of the Cluster SC3 measurements and the GUMICS–4 simulations are poor in the solar wind (see Table 7). The B_z , the V_x , the n_{CIS} and the n_{EFW} are the magnetic field GSE Z component, the plasma ion velocity X GSE component, the solar wind density measured by the CIS HIA instrument and the calculated from the EFW spacecraft potential, respectively. (a, b, c) Distribution of OMNI V_x , V_y , V_z when the agreement of B_z is poor. (d, e, f) Distribution of OMNI V_x , V_y , V_z when the agreement of V_x is poor. (g, h, i) Distribution of OMNI V_x , V_y , V_z when the agreement of n_{CIS} is poor. (j, k, l) Distribution of OMNI V_x , V_y , V_z when the agreement of n_{EFW} is poor. The values are in percentage unit in the distributions. The red distributions of (a, d, g, j), (b, e, h, k) and (c, f, i, l) are the distributions of the V_x , the V_y and the V_z components of the OMNI solar wind velocity during the 1-year run from January 29, 2002 to February 2, 2003 in GSE reference frame, respectively.



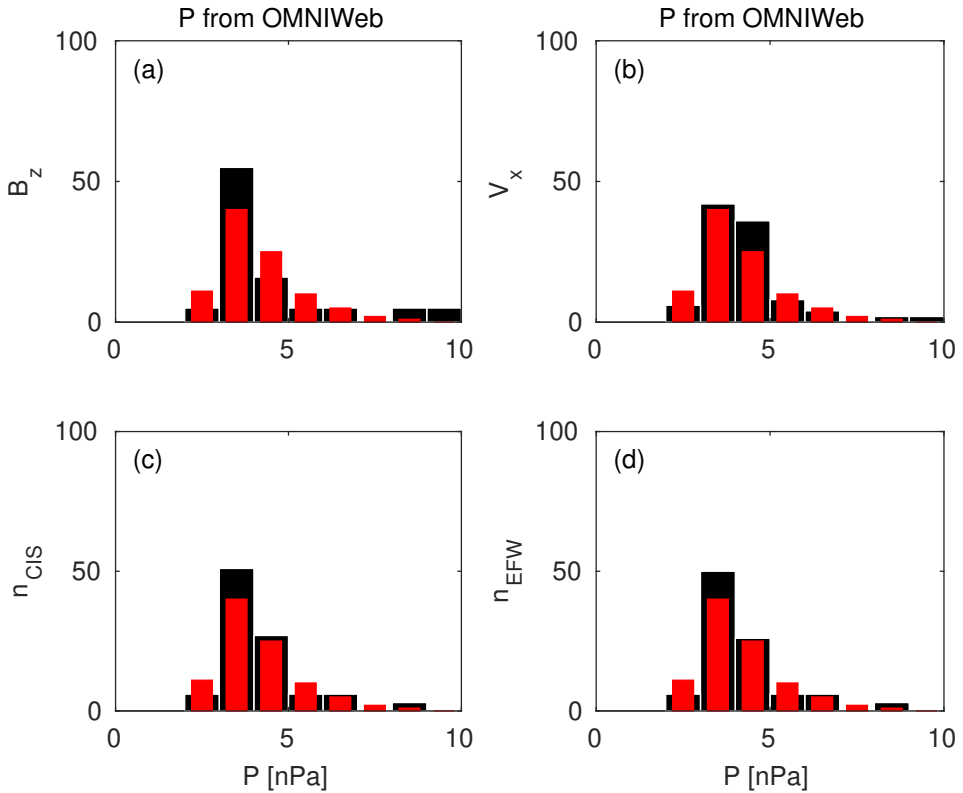
999 **Figure 16.** The black distributions of the P solar wind dynamic pressure calculated from
1000 OMNI parameters when the agreement of the Cluster SC3 measurements and the GUMICS-4
1001 simulations are poor in the solar wind (see Table 7). The B_z , V_x , n_{CIS} and n_{EFW} are the mag-
1002 netic field GSE Z component, the velocity X GSE component, the solar wind density measured
1003 by the CIS HIA instrument and calculated from the EFW spacecraft potential, respectively.
1004 (a, b, c, d) The distribution of the P calculated from OMNI data when the agreement of the B_z ,
1005 the V_x , the n_{CIS} or the n_{EFW} are poor. The values are in percentage unit in the distributions.
1006 The red distributions of (a, b, c, d) are the distributions of the P solar wind dynamic pressure
1007 calculated from the OMNI solar wind parameters during the 1-year run from January 29, 2002 to
1008 February 2, 2003 in GSE reference frame.



1009 **Figure 17.** The black distributions of the B_x , the B_y and the B_z OMNI solar wind magnetic
 1010 field components when the agreement of the Cluster SC3 measurements and the GUMICS–4
 1011 simulations are poor in the magnetosheath (see Table 8). The B_z , the V_x , the n_{CIS} and the
 1012 n_{EFW} are the magnetic field GSE Z component, the plasma ion velocity X GSE component,
 1013 the solar wind density measured by the CIS HIA instrument and the calculated from the EFW
 1014 spacecraft potential, respectively. (a, b, c) Distribution of OMNI B_x , B_y , B_z when the agree-
 1015 ment of B_z is poor. (d, e, f) Distribution of OMNI B_x , B_y , B_z when the agreement of V_x is
 1016 poor. (g, h, i) Distribution of OMNI B_x , B_y , B_z when the agreement of n_{CIS} is poor. (j, k, l)
 1017 Distribution of OMNI B_x , B_y , B_z when the agreement of n_{EFW} is poor. The values are in per-
 1018 centage unit in the distributions. The red distributions of (a, d, g, j), (b, e, h, k) and (c, f, i, l)
 1019 are the distribution of the B_x , the B_y , and the B_z components of the OMNI solar wind magnetic
 1020 field during the 1-year run from January 29, 2002 to February 2, 2003 in GSE reference frame,
 1021 respectively.



1022 **Figure 18.** The black distributions of the V_x , the V_y and the V_z OMNI solar wind magnetic
 1023 field components when the agreement of the Cluster SC3 measurements and the GUMICS-4
 1024 simulations are poor in the magnetosheath (see Table 8). The B_z , the V_x , the n_{CIS} and the
 1025 n_{EFW} are the magnetic field GSE Z component, the plasma ion velocity X GSE component, the
 1026 solar wind density measured by the CIS HIA instrument and the calculated from the EFW space-
 1027 craft potential, respectively. (a, b, c) Distribution of OMNI V_x , V_y , V_z when the agreement of
 1028 B_z is poor. (d, e, f) Distribution of OMNI V_x , V_y , V_z when the agreement of V_x is poor. (g, h, i)
 1029 Distribution of OMNI V_x , V_y , V_z when the agreement of n_{CIS} is poor. (j, k, l) Distribution of
 1030 OMNI V_x , V_y , V_z when the agreement of n_{EFW} is poor. The values are in percentage unit in the
 1031 distributions. The red distributions of (a, d, g, j), (b, e, h, k) and (c, f, i, l) are the distributions
 1032 of the V_x , the V_y and the V_z components of the OMNI solar wind velocity during the 1-year run
 1033 from January 29, 2002 to February 2, 2003 in GSE reference frame, respectively.



1034 **Figure 19.** The black distributions of the P solar wind dynamic pressure calculated from
 1035 OMNI parameters when the agreement of the Cluster SC3 measurements and the GUMICS–4
 1036 simulations are poor in the magnetosheath (see Table 8). The B_z , V_x , n_{CIS} and n_{EFW} are
 1037 the magnetic field GSE Z component, the velocity X GSE component, the solar wind density
 1038 measured by the CIS HIA instrument and calculated from the EFW spacecraft potential, respec-
 1039 tively. (a, b, c, d) The distribution of the P calculated from OMNI data when the agreement of
 1040 the B_z , the V_x , the n_{CIS} or the n_{EFW} are poor. The values are in percentage unit in the distri-
 1041 butions. The red distributions of (a, b, c, d) are the distributions of the P solar wind dynamic
 1042 pressure calculated from the OMNI solar wind parameters during the 1-year run from January
 1043 29, 2002 to February 2, 2003 in GSE reference frame.

Start/End	C_{B_z}	δt_{B_z}	C_{V_x}	δt_{V_x}	$C_{n_{CIS}}$	$\delta t_{n_{CIS}}$	$C_{n_{EFW}}$	$\delta t_{n_{EFW}}$
	[min]		[min]		[min]		[min]	
20020201 20:00/0203 04:00	0.97	3	1.00	12	0.96	3	0.98	3
20020211 13:00/0212 12:00	0.86	2	1.00	0	0.99	19	0.99	18
20020218 09:00/0219 02:00	0.95	1	1.00	-4	1.00	-3	0.97	-2
20020219 06:30/0219 15:00	0.96	1	0.99	-1	0.99	-60	1.00	60
20020220 18:30/0222 00:00	0.90	4	1.00	4	0.93	-20	0.98	3
20020318 17:30/0319 02:30	0.91	2	1.00	21	0.98	51	0.99	6
20020412 20:30/0413 02:00	0.91	5	0.99	-53	0.94	60	0.98	12
20021227 12:00/1228 03:00	0.84	4	1.00	-2	0.99	-21	0.99	22
20021229 20:00/1230 16:00	0.76	1	1.00	1	0.99	-30	0.98	43
20030106 06:00/0106 19:00	0.82	5	1.00	7	0.99	3	0.95	-60
20030108 07:00/0109 03:30	0.56	10	1.00	41	0.99	9	0.97	-56
20030113 08:30/0113 18:00	0.94	3	1.00	5	1.00	3	0.97	-1
20030120 07:30/0120 13:00	0.86	3	1.00	8	1.00	4	1.00	-55
20030122 12:00/0123 14:00	0.85	2	1.00	3	1.00	3	0.92	-60
20030124 18:00/0126 00:00	0.78	3	1.00	0	0.99	-60	0.99	60
20030127 16:00/0128 06:00	0.89	-1	1.00	-3	0.96	1	0.89	12
20030129 12:00/0130 18:00	0.92	2	1.00	4	0.95	-59	0.98	1

Table 1. The studied solar wind intervals. The correlation coefficients (C_{B_z} , C_{V_x} , $C_{n_{CIS}}$, $C_{n_{EFW}}$) and time shift (δt_{V_x} , $\delta t_{n_{CIS}}$, $\delta t_{n_{EFW}}$) in minutes of the magnetic field GSE Z component (B_z), solar wind velocity X component (V_x), CIS and EFW densities (n_{CIS} , n_{EFW}).

Table 2: The studied magnetosheath intervals. The correlation coefficients (C_{B_z} , C_{V_x} , $C_{n_{CIS}}$, $C_{n_{EFW}}$) and time shift (δt_{V_x} , $\delta t_{n_{CIS}}$, $\delta t_{n_{EFW}}$) in minutes of the magnetic field GSE Z component (B_z), solar wind velocity X component (V_x), CIS and EFW densities (n_{CIS} , n_{EFW}). In the empty slots the correlation calculation gives invalid result.

Start/End	C_{B_z}	δt_{B_z}	C_{V_x}	δt_{V_x}	$C_{n_{CIS}}$	$\delta t_{n_{CIS}}$	$C_{n_{EFW}}$	$\delta t_{n_{EFW}}$
		[min]		[min]		[min]		[min]
20020201 13:30/0201 18:30	0.92	1	0.98	57	0.99	60	0.98	60
20020208 18:15/0209 00:00	0.78	3	0.95	60	0.98	-53	0.98	-54
20020211 02:30/0211 09:00	0.81	0	0.99	-21	1.00	0	0.99	0
20020212 16:30/0212 21:00	0.86	3	1.00	54	0.99	30	0.99	30
20020219 17:30/0219 23:00	0.78	4	0.99	37	1.00	6	1.00	6
20020222 23:00/0223 06:30	0.69	1	0.97	-60	0.99	-52	0.99	-48
20020227 16:30/0227 23:15	0.53	60	0.98	-31	1.00	-38	1.00	-11
20020310 18:30/0311 00:30	0.98	3	0.98	20	0.99	8	0.99	-2
20020311 14:00/0311 19:00	0.88	5	0.97	36	0.99	-3	0.99	-40
20020406 19:00/0407 01:15	0.79	1	0.97	-60	0.98	-56	0.98	-56
20020410 17:30/0410 23:00	0.89	5	0.99	-52	1.00	3	1.00	5
20020411 11:30/0411 16:30	0.84	3	0.99	40	0.99	3	0.99	3
20020418 18:30/0418 22:45	0.93	59	0.99	-60	0.99	60	0.98	60
20020421 04:30/0421 07:45	0.98	55	1.00	-60	1.00	-60	1.00	-60
20020422 11:45/0422 15:45	0.77	-5	0.98	-17	0.99	-15	0.99	-16
20020423 08:30/0423 12:30	0.94	31	1.00	4	0.99	16	1.00	16
20020430 12:30/0430 17:00	0.81	58	0.99	23	0.99	-18		
20020505 07:00/0505 11:15	0.83	59	0.99	32	0.99	-60		
20020506 19:15/0507 00:15	0.89	-28	0.99	-60	0.98	-36		
20020507 17:30/0507 23:00	0.94	1	0.99	47	0.99	-47		
20020514 22:45/0515 03:00	0.82	49	0.99	-60	0.99	32	0.99	-37
20020517 07:00/0517 12:15	0.76	-6	1.00	-5	0.99	-4	0.99	-3
20020518 13:30/0518 19:30	0.76	1	0.99	11	0.98	-2	0.98	-2

Continued on next page

Table 2 – *Continued from previous page*

Start/End	C_{B_z}	δt_{B_z}	C_{V_x}	δt_{V_x}	$C_{n_{CIS}}$	$\delta t_{n_{CIS}}$	$C_{n_{EFW}}$	$\delta t_{n_{EFW}}$
		[min]		[min]		[min]		[min]
20020519 20:00/0520 03:30	0.98	2	1.00	-9	0.99	-4	0.99	-50
20020520 10:45/0520 20:15	0.80	1	0.99	-3	0.95	-1	0.99	-1
20020522 02:00/0522 08:45	0.53	52	0.99	4	0.99	11	0.99	22
20020527 02:15/0527 17:15	0.80	-3	0.99	-2	0.98	0	0.99	0
20020530 05:00/0530 10:30	0.30	3	1.00	-23	0.99	4	0.99	3
20020601 19:30/0602 01:00	0.68	-2	1.00	17	0.99	-6	0.99	-7
20020602 21:45/0603 17:45	0.65	-5	0.99	0	0.98	3	0.99	3
20020605 10:30/0606 06:00	0.20	0	0.99	-7	0.98	10	0.98	9
20020607 18:00/0607 22:00	0.93	-35	1.00	-34	0.99	16	0.99	15
20020608 01:15/0608 18:15	0.54	-4	1.00	-39	0.97	-6	0.97	-6
20020610 01:30/0610 09:30	0.80	5	1.00	8	0.99	3	1.00	-7
20020610 11:00/0611 01:00	0.89	-4	1.00	-35	0.99	24	0.99	7
20020612 18:30/0613 06:15	0.45	-2	0.99	-7	0.97	-3	0.97	-33
20020615 07:00/0615 23:30			1.00	47	0.98	-3	0.98	-5
20020617 05:00/0618 03:45	0.79	3	1.00	28	0.98	9	0.99	8
20020620 04:00/0620 11:00	0.65	-8	0.99	-6	0.98	11	0.98	6
20020622 14:30/0622 18:00	0.99	56	1.00	33	1.00	16	1.00	16
20021201 04:15/1202 07:45	0.41	1	1.00	2	0.99	6	0.99	6
20021203 15:30/1204 19:30	0.72	1	0.99	60	0.98	59	0.98	59
20021207 00:30/1207 07:45	0.53	38	0.99	-50	0.99	-20	0.99	20
20021208 09:30/1209 08:00	0.72	3	0.99	-36	0.98	5	0.98	5
20021212 23:30/1213 14:30	0.53	5	1.00	36	0.99	-3	0.95	-56
20021213 21:15/1214 09:30	0.96	5	1.00	-35	0.99	-5	0.99	-46
20021215 12:45/1216 18:00	0.80	2	0.99	-60	0.95	-60	0.98	30
20021217 16:30/1218 01:45	0.91	2	1.00	-54	0.99	3	0.99	3
20021220 01:30/1220 06:15	0.93	0	1.00	60	0.99	2	0.99	3
20021223 02:15/1223 13:00	0.93	1	0.97	39	0.94	50	0.99	-14
20021223 14:00/1223 22:30	0.88	1	1.00	-2	0.99	-1	1.00	-3
20021224 19:00/1225 01:45	0.96	0	1.00	-43	0.99	12	0.99	28

Continued on next page

Table 2 – *Continued from previous page*

Start/End	C_{B_z}	δt_{B_z}	C_{V_x}	δt_{V_x}	$C_{n_{CIS}}$	$\delta t_{n_{CIS}}$	$C_{n_{EFW}}$	$\delta t_{n_{EFW}}$
		[min]		[min]		[min]		[min]
20021225 23:45/1226 07:15	0.97	7	1.00	-18	0.99	56	0.99	56
20021226 23:00/1227 09:45	0.83	2	1.00	2	0.99	4	0.99	2
20021229 11:45/1229 17:00	0.63	2	1.00	-32	0.99	49	0.99	48
20021230 17:45/1231 01:00	0.74	1	0.99	55	0.98	60	0.98	22
20021231 23:00/0101 05:15	0.92	2	1.00	0	0.99	-54	1.00	-56
20030105 14:00/0105 21:00	0.73	1	1.00	1	1.00	-60	0.99	-60
20030106 23:15/0107 03:00	0.70	4	0.99	41	1.00	56	1.00	-60
20030109 08:45/0109 16:15			0.91	-55	0.98	-13	0.98	-25
20030110 07:15/0110 15:15	0.95	1	0.99	-7	0.99	2	0.98	11
20030111 08:15/0111 22:30	0.88	1	0.99	-59	0.94	-15	0.94	8
20030112 17:30/0113 00:15	0.98	0	1.00	-47	0.99	39	0.99	51
20030114 00:30/0114 08:30	0.86	-1	0.99	-60	0.98	23	0.98	8
20030116 10:15/0116 17:45	0.64	60	0.93	52	0.99	60	0.99	30
20030117 09:30/0117 13:30	0.70	-3	1.00	7	1.00	-31	1.00	-33
20030118 23:30/0119 03:45	0.97	3	1.00	-12	1.00	7	0.99	7
20030119 21:00/0120 01:00	0.96	3	1.00	6	1.00	38	1.00	20
20030121 06:30/0121 11:30	0.87	-3	0.98	40	0.99	8	1.00	8
20030122 04:45/0122 09:30	0.76	-2	1.00	1	1.00	-7	1.00	-4
20030126 01:45/0126 06:30	0.90	3	0.99	-15	1.00	-51	0.99	24
20030127 08:15/0127 13:00	1.00	10	1.00	-60	0.99	-1	0.99	1
20030128 12:30/0128 17:15	0.77	60	0.99	-22	0.99	-5	0.99	21
20030130 19:45/0131 00:15	0.98	2	0.99	52	0.99	8	0.99	8

Table 3: The studied magnetosphere intervals (UT).

Start/End
20020213 23:00/0214 01:30
20020217 18:30/0218 02:00
20020220 00:45/0220 12:00
20020222 11:15/0222 20:15
20020225 02:15/0225 08:30
20020227 06:00/0227 12:00
20020302 00:00/0302 03:15
20020306 10:00/0306 18:30
20020308 17:30/0309 06:00
20020311 02:15/0311 12:00
20020313 11:15/0314 00:15
20020316 04:45/0316 08:00
20020318 09:00/0318 14:45
20020320 20:30/0320 23:55
20020323 04:00/0323 09:45
20020327 23:45/0328 06:15
20020330 07:15/0330 12:45
20020401 19:30/0401 22:00
20020406 09:30/0406 18:00
20020408 15:00/0409 00:00
20020410 23:30/0411 09:45
20020413 08:30/0413 19:00
20020416 18:00/0417 04:30
20020418 06:00/0418 12:00
20020420 15:00/0420 23:00
20020422 20:00/0423 07:00
20020425 08:30/0425 18:00
20020430 04:40/0430 12:00
20020504 14:30/0504 16:45

Continued on next page

Table 3 – *Continued from previous page*

Start/End
20020505 02:30/0505 07:00
20020507 01:30/0507 15:45
20020508 11:00/0510 04:15
20020512 02:45/0512 09:30
20020514 10:30/0514 12:45
20020519 00:30/0519 19:30
20020521 01:30/0521 22:00
20020523 23:30/0524 02:00
20020524 19:00/0525 08:15
20020526 07:30/0526 10:30
20020528 20:00/0529 05:00
20020531 02:15/0531 13:30
20020602 04:30/0602 07:30
20020602 12:00/0602 21:30
20020604 08:30/0605 07:00
20020606 14:30/0607 16:30
20020609 06:00/0609 20:00
20020611 11:00/0612 13:00
20020614 01:00/0614 16:00
20020616 08:00/0616 18:00
20020620 13:30/0622 01:00
20020623 13:00/0623 17:00
20020624 04:00/0624 10:15
20020630 17:45/0701 15:00
20020701 21:00/0703 10:30
20020703 23:00/0706 03:15
20020707 01:00/0708 23:00
20020710 11:30/0714 03:30
20020714 15:45/0715 15:30
20020716 23:30/0717 16:00

Continued on next page

Table 3 – *Continued from previous page*

Start/End
20020718 05:45/0722 11:00
20020722 23:45/0728 01:00
20020728 02:00/0804 03:45
20020804 04:45/0811 06:15
20020811 07:30/0816 01:00
20020816 15:30/0818 09:00
20020818 10:00/0825 11:30
20020825 13:00/0901 14:15
20020901 17:15/0903 23:30
20020905 02:15/0906 16:30
20020907 10:30/0908 17:00
20020908 18:00/0915 19:30
20020915 21:00/0922 22:30
20020923 00:00/0923 23:30
20020924 03:30/0928 22:45
20020928 23:30/0930 01:00
20020930 02:15/1006 17:00
20021006 17:45/1007 03:30
20021007 05:00/1007 17:30
20021008 07:30/1010 22:00
20021010 22:30/1012 22:30
20021012 23:00/1014 06:30
20021014 09:00/1016 04:00
20021016 14:00/1019 00:15
20021019 01:30/1019 22:00
20021021 04:00/1022 19:30
20021022 22:30/1026 02:30
20021026 04:00/1029 20:15
20021030 01:30/1102 08:00
20021102 22:00/1104 22:00

Continued on next page

Table 3 – *Continued from previous page*

Start/End
20021106 00:00/1107 18:00
20021108 02:00/1109 18:45
20021111 00:00/1112 01:30
20021113 03:45/1114 14:15
20021115 20:30/1116 23:00
20021118 01:00/1118 23:30
20021120 17:00/1121 06:00
20021122 21:30/1124 01:00
20021125 04:00/1126 08:30
20021127 20:00/1128 18:30
20021130 04:00/1201 01:30
20021202 14:30/1203 09:00
20021204 22:00/1205 19:30
20021207 09:00/1207 16:30
20021207 18:00/1207 22:00
20021209 16:30/1210 14:30
20021212 13:45/1212 21:30
20021214 13:30/1214 20:00
20021214 21:00/1215 07:30
20021216 21:00/1217 15:00
20021219 08:00/1219 19:30
20021221 15:45/1221 23:15
20021222 00:30/1222 08:45
20021224 02:30/1224 14:00
20021226 10:00/1226 19:00
20021228 19:30/1229 02:30
20021229 04:00/1229 10:00
20021231 05:00/1231 18:45
20030102 12:30/0102 20:45
20030104 20:45/0105 06:00

Continued on next page

Table 3 – *Continued from previous page*

Start/End
20030105 07:00/0105 13:30
20030107 05:45/0107 21:00
20030109 17:00/0110 00:45
20030112 00:00/0112 09:15
20030112 10:30/0112 16:00
20030114 11:00/0114 20:00
20030116 20:30/0116 22:45
20030119 04:30/0119 09:30
20030119 14:00/0119 17:00
20030121 13:30/0121 21:30
20030126 07:30/0126 15:45
20030128 17:45/0129 08:15
20030131 01:30/0131 11:45

Table 4: Intervals around the studied bow shock crossings. The Cluster SC3 crossed the bow shock in all cases. The 2nd column shows whether the bow shock is visible in the GUMICS–4 simulations.

Start/End	GUMICS Bow Shock
20020201 12:00/0202 00:00	+
20020203 00:00/0203 12:00	+
20020206 06:00/0206 18:00	+
20020208 18:00/0209 06:00	+
20020211 06:00/0211 18:00	+
20020212 12:00/0212 18:00	+
20020213 12:00/0213 18:00	+
20020216 00:00/0216 12:00	+
20020217 06:00/0217 12:00	-
20020218 06:00/0218 18:00	+
20020219 00:00/0219 18:00	+
20020220 12:00/0221 00:00	+
20020221 18:00/0222 00:00	+
20020301 06:00/0301 12:00	+
20020304 12:00/0304 18:00	+
20020306 00:00/0306 06:00	+
20020307 00:00/0307 06:00	+
20020308 06:00/0308 12:00	+
20020309 06:00/0309 12:00	+
20020310 12:00/0311 00:00	+
20020311 18:00/0312 00:00	+
20020313 00:00/0313 06:00	-
20020314 00:00/0314 12:00	+
20020316 06:00/0316 18:00	+
20020318 12:00/0319 00:00	+
20020323 12:00/0323 18:00	+

Continued on next page

Table 4 – *Continued from previous page*

Start/End	GUMICS Bow Shock
20020325 18:00/0326 06:00	–
20020327 06:00/0327 12:00	+
20020329 18:00/0330 00:00	–
20020402 00:00/0402 06:00	+
20020405 18:00/0406 00:00	–
20020407 00:00/0407 06:00	–
20020409 06:00/0409 12:00	–
20020410 12:00/0410 18:00	–
20020411 12:00/0411 18:00	–
20020413 00:00/0413 06:00	+
20020413 18:00/0414 06:00	+
20020420 00:00/0420 06:00	+
20020423 12:00/0423 23:00	+
20020427 00:00/0427 06:00	+
20020428 06:00/0428 12:00	+
20020430 18:00/0501 00:00	+
20020505 06:00/0505 18:00	–
20020507 18:00/0509 06:00	+
20020510 06:00/0510 12:00	+
20020513 12:00/0513 18:00	+
20020515 00:00/0515 06:00	–
20020520 00:00/0520 06:00	+
20020522 06:00/0522 12:00	+
20020522 18:00/0523 06:00	+
20021206 06:00/1207 06:00	+
20021218 00:00/1219 00:00	+
20021220 18:00/1221 00:00	+
20021221 00:00/1221 12:00	+
20021222 12:00/1223 00:00	+
20021223 00:00/1223 06:00	+

Continued on next page

Table 4 – *Continued from previous page*

Start/End	GUMICS Bow Shock
20021225 06:00/1226 00:00	+
20021227 06:00/1228 00:00	+
20021228 00:00/1228 12:00	+
20021229 12:00/1230 00:00	+
20030101 06:00/0102 00:00	+
20030103 06:00/0103 12:00	+
20030104 00:00/0104 18:00	+
20030106 00:00/0107 00:00	+
20030108 00:00/0108 12:00	+
20030113 00:00/0114 06:00	+
20030115 00:00/0115 12:00	+
20030118 18:00/0119 00:00	+
20030120 00:00/0121 12:00	+
20030122 06:00/0122 12:00	+
20030123 12:00/0124 00:00	+
20030124 12:00/0124 18:00	+
20030126 00:00/0126 06:00	+
20030127 00:00/0127 18:00	+
20030128 06:00/0128 18:00	+
20030129 06:00/0129 12:00	+
20030130 18:00/0131 00:00	+

Table 5: Intervals around the studied magnetopause crossings.
The Cluster SC3 crossed the magnetopause in all cases. The
2nd column shows whether the magnetopause is visible in the
GUMICS–4 simulations.

Start/End	GUMICS Magnetopause
20020203 06:00/0203 12:00	+
20020206 06:00/0206 12:00	-
20020211 00:00/0211 06:00	+
20020218 00:00/0218 06:00	+
20020225 06:00/0225 12:00	+
20020302 00:00/0302 06:00	+
20020306 18:00/0307 00:00	-
20020308 12:00/0308 18:00	-
20020311 12:00/0311 18:00	+
20020313 18:00/0314 00:00	-
20020314 00:00/0314 06:00	+
20020323 06:00/0323 12:00	+
20020330 12:00/0330 18:00	-
20020404 06:00/0404 12:00	-
20020409 00:00/0409 06:00	-
20020418 12:00/0418 18:00	+
20020422 12:00/0422 18:00	-
20020429 18:00/0430 00:00	-
20020507 12:00/0507 18:00	-
20020509 06:00/0509 12:00	-
20020510 00:00/0510 06:00	-
20020514 18:00/0515 00:00	-
20020519 12:00/0519 18:00	-
20020520 12:00/0521 00:00	-
20020522 00:00/0522 06:00	-
20020529 00:00/0529 12:00	-

Continued on next page

Table 5 – *Continued from previous page*

Start/End	GUMICS Magnetopause
20020530 06:00/0530 18:00	–
20020531 18:00/0601 00:00	–
20020602 18:00/0603 00:00	–
20020604 06:00/0604 12:00	–
20020605 06:00/0606 18:00	–
20020607 12:00/0608 06:00	+
20020609 00:00/0609 06:00	–
20020610 00:00/0610 06:00	–
20020611 00:00/0611 12:00	–
20020612 06:00/0614 00:00	–
20020614 18:00/0615 06:00	–
20020616 00:00/0616 12:00	+
20020620 00:00/0620 18:00	–
20020622 06:00/0622 18:00	–
20020704 12:00/0705 00:00	–
20020706 00:00/0706 12:00	+
20020709 00:00/0709 18:00	–
20020715 18:00/0716 12:00	–
20030105 06:00/0105 18:00	+
20030110 00:00/0110 12:00	+
20030112 12:00/0112 18:00	–
20030117 06:00/0117 12:00	+
20030121 06:00/0121 12:00	+
20030122 00:00/0122 06:00	–
20030126 18:00/0127 00:00	+
20030128 12:00/0128 18:00	+
20030129 00:00/0129 12:00	+
20030131 12:00/0201 00:00	+

Start/End	GUMICS Neutral Sheet
20020901 19:00/0902 00:00	–
20020906 14:00/0906 16:30	+
20020913 17:30/0913 20:00	+
20020918 13:00/0918 14:30	–
20020920 20:30/0921 02:00	+
20020928 03:00/0928 07:00	+
20021002 16:00/1003 00:00	–
20021014 12:30/1014 23:00	+
20021017 03:00/1017 04:00	–

1051 **Table 6.** Intervals around the studied neutral sheet crossings in the tail. The Cluster SC3
 1052 crossed the neutral sheet in all cases. The 2nd column shows whether the neutral sheet is visible
 1053 in the GUMICS–4 simulations.

Start/End	OMNI			Cluster SC3			
	B_z [nT]	V_x [km/s]	P [cm $^{-3}$]	B_z	V_x	n_{CIS}	n_{EFW}
20020201 20:00/0203 04:00	-1.25	-373.52	4.08	y	y	n	y
20020211 13:00/0212 12:00	0.03	-533.11	2.18	y	y	y	y
20020218 09:00/0219 02:00	2.56	-362.41	3.46	y	n	n	y
20020219 06:30/0219 15:00	3.55	-401.63	1.25	y	y	n	n
20020220 18:30/0222 00:00	1.95	-440.18	1.96	y	y	n	y
20020318 17:30/0319 02:30	3.79	-429.30	15.34	y	n	n	n
20020412 20:30/0413 02:00	-1.81	-420.35	3.24	y	n	n	y
20021227 12:00/1228 03:00	0.09	-714.40	2.72	y	n	n	y
20021229 20:00/1230 16:00	-0.37	-526.40	2.26	y	y	n	n
20030106 06:00/0106 19:00	2.25	-399.91	1.50	y	n	n	n
20030108 07:00/0109 03:30	-0.58	-280.80	2.97	n	n	y	n
20030113 08:30/0113 18:00	0.68	-397.83	1.72	y	y	y	n
20030120 07:30/0120 13:00	2.16	-630.69	2.43	y	y	y	y
20030122 12:00/0123 14:00	0.13	-608.96	3.41	y	y	y	n
20030124 18:00/0126 00:00	-0.71	-739.68	2.87	y	y	n	n
20030127 16:00/0128 06:00	-0.92	-451.84	3.12	y	y	n	n
20030129 12:00/0130 18:00	-3.09	-450.00	3.96	y	y	n	y

1054 **Table 7.** The average OMNI input parameters in the solar wind and the good/bad agreement
 1055 of the GUMICS–4 simulations to the Cluster B_z magnetic field component, the V_x solar wind
 1056 speed component, the n_{CIS} solar wind density measured by the Cluster CIS HIA instrument and
 1057 the n_{EFW} solar wind density calculated from the spacecraft potential measured by the Cluster
 1058 EFW instrument in the solar wind.

Table 8: The average OMNI input parameters in the solar wind and the good/bad agreement of the GUMICS–4 simulations to the Cluster B_z magnetic field component, the V_x solar wind speed component, the n_{CIS} solar wind density measured by the Cluster CIS HIA instrument and the n_{EFW} solar wind density calculated from the spacecraft potential measured by the Cluster EFW instrument in the magnetosheath.

Start/End	OMNI			Cluster SC3			
	B_z	V_x	P	B_z	V_x	n_{CIS}	n_{EFW}
	[nT]	[km/s]	[cm $^{-3}$]				
20020201 13:30/0201 18:30	0.19	-342.87	4.62	y	n	n	n
20020208 18:15/0209 00:00	-0.48	-508.16	1.61	y	n	n	n
20020211 02:30/0211 09:00	-1.85	-425.67	1.78	y	y	y	y
20020212 16:30/0212 21:00	2.98	-509.22	2.34	y	n	n	n
20020219 17:30/0219 23:00	1.46	-431.50	1.46	y	y	y	y
20020222 23:00/0223 06:30	0.86	-391.22	1.14	y	n	n	n
20020227 16:30/0227 23:15	1.89	-343.13	1.52	n	n	n	n
20020310 18:30/0311 00:30	-2.81	-379.46	1.78	y	y	y	y
20020311 14:00/0311 19:00	1.63	-371.43	2.68	n	n	n	n
20020406 19:00/0407 01:15	-2.71	-333.13	0.93	y	n	n	n
20020410 17:30/0410 23:00	0.31	-312.43	4.42	n	n	y	y
20020411 11:30/0411 16:30	-1.50	-494.02	4.25	y	y	n	n
20020418 18:30/0418 22:45	-0.92	-450.82	0.30	n	n	n	n
20020421 04:30/0421 07:45	0.40	-455.69	1.37	n	n	n	n
20020422 11:45/0422 15:45	0.25	-419.98	1.14	n	n	y	y
20020423 08:30/0423 12:30	2.77	-507.99	6.82	n	n	n	n
20020430 12:30/0430 17:00	2.15	-479.51	3.02	n	n	n	n
20020505 07:00/0505 11:15	0.20	-336.81	1.74	n	n	n	n
20020506 19:15/0507 00:15	0.78	-390.00	2.46	y	n	n	n
20020507 17:30/0507 23:00	2.87	-392.40	3.49	y	n	n	n
20020514 22:45/0515 03:00	-2.42	-414.01	1.82	n	n	n	n

Continued on next page

Table 8 – *Continued from previous page*

Start/End	OMNI			Cluster SC3			
	B_z [nT]	V_x [km/s]	P $[cm^{-3}]$	B_z	V_x	n_{CIS}	n_{EFW}
20020517 07:00/0517 12:15	-0.39	-379.32	1.52	y	y	y	y
20020518 13:30/0518 19:30	0.63	-345.87	1.59	n	n	y	y
20020519 20:00/0520 03:30	4.75	-408.56	1.12	y	y	y	y
20020520 10:45/0520 20:15	0.74	-448.89	1.93	y	y	y	y
20020522 02:00/0522 08:45	-1.07	-398.12	1.63	n	y	y	y
20020527 02:15/0527 17:15	-3.11	-542.53	2.07	y	y	y	y
20020530 05:00/0530 10:30	0.03	-493.86	2.08	y	n	y	y
20020601 19:30/0602 01:00	-3.38	-342.27	4.16	y	y	y	y
20020602 21:45/0603 17:45	0.38	-435.47	1.89	y	y	y	y
20020605 10:30/0606 06:00	-0.42	-394.49	1.08	y	y	n	n
20020607 18:00/0607 22:00	-1.60	-291.85	1.80	y	y	y	y
20020608 01:15/0608 18:15	0.06	-335.39	2.74	y	n	y	y
20020610 01:30/0610 09:30	1.60	-465.52	3.00	y	y	y	y
20020610 11:00/0611 01:00	-2.27	-419.86	2.16	y	n	y	y
20020612 18:30/0613 06:15	-1.13	-351.03	1.16	y	y	y	y
20020615 07:00/0615 23:30	-1.16	-334.27	2.84	n	n	y	y
20020617 05:00/0618 03:45	0.78	-351.47	1.87	y	n	y	y
20020620 04:00/0620 11:00	0.46	-485.48	1.73	y	y	y	y
20020622 14:30/0622 18:00	-0.72	-429.02	1.93	n	n	y	y
20021201 04:15/1202 07:45	-1.09	-499.23	2.62	y	y	y	y
20021203 15:30/1204 19:30	0.34	-449.09	2.06	y	n	n	n
20021207 00:30/1207 07:45	0.80	-451.80	7.33	n	n	y	y
20021208 09:30/1209 08:00	0.60	-600.27	1.49	y	n	y	y
20021212 23:30/1213 14:30	0.10	-337.77	1.32	y	n	n	n
20021213 21:15/1214 09:30	-0.74	-361.19	2.99	y	n	y	y
20021215 12:45/1216 18:00	1.32	-479.48	1.53	y	n	n	n
20021217 16:30/1218 01:45	4.56	-393.99	2.49	y	n	y	y
20021220 01:30/1220 06:15	-1.21	-530.62	3.01	y	n	y	y

Continued on next page

Table 8 – *Continued from previous page*

Start/End	OMNI			Cluster SC3			
	B_z [nT]	V_x [km/s]	P $[cm^{-3}]$	B_z	V_x	n_{CIS}	n_{EFW}
20021223 02:15/1223 13:00	-2.32	-516.12	2.22	y	n	n	n
20021223 14:00/1223 22:30	0.89	-519.77	2.55	y	y	y	y
20021224 19:00/1225 01:45	0.88	-523.86	3.41	y	n	y	y
20021225 23:45/1226 07:15	-0.61	-414.38	2.21	y	y	n	n
20021226 23:00/1227 09:45	-1.79	-618.14	6.20	y	y	y	y
20021229 11:45/1229 17:00	-0.41	-580.12	2.39	y	n	n	n
20021230 17:45/1231 01:00	-1.01	-483.60	1.93	y	n	n	y
20021231 23:00/0101 05:15	0.60	-418.95	1.94	y	n	n	n
20030105 14:00/0105 21:00	-0.03	-414.46	1.69	y	n	n	n
20030106 23:15/0107 03:00	-1.62	-392.29	1.56	n	n	n	n
20030109 08:45/0109 16:15	1.45	-272.82	2.31	n	n	n	n
20030110 07:15/0110 15:15	-2.11	-401.03	2.72	y	n	y	y
20030111 08:15/0111 22:30	-0.20	-433.33	1.24	y	n	n	y
20030112 17:30/0113 00:15	1.53	-389.62	1.45	y	n	n	n
20030114 00:30/0114 08:30	-1.67	-388.53	2.27	y	n	n	y
20030116 10:15/0116 17:45	-1.20	-328.91	1.22	n	n	n	n
20030117 09:30/0117 13:30	-1.36	-327.09	2.55	y	y	y	y
20030118 23:30/0119 03:45	6.41	-459.46	4.82	y	y	y	y
20030119 21:00/0120 01:00	1.52	-597.95	2.38	y	n	y	y
20030121 06:30/0121 11:30	-1.77	-670.25	1.50	y	n	n	n
20030122 04:45/0122 09:30	0.11	-588.87	2.30	y	n	y	y
20030126 01:45/0126 06:30	-0.24	-713.82	2.75	y	y	y	y
20030127 08:15/0127 13:00	7.94	-509.30	0.47	y	n	y	y
20030128 12:30/0128 17:15	4.95	-443.83	4.15	y	y	y	y
20030130 19:45/0131 00:15	4.21	-510.33	2.63	y	n	y	y